



Contents lists available at ScienceDirect

Journal of Rock Mechanics and Geotechnical Engineering

journal homepage: www.jrmge.cn

Qian Lecture

Excavation-induced deep hard rock fracturing: Methodology and applications

Xia-Ting Feng*, Cheng-Xiang Yang, Rui Kong, Jun Zhao, Yangyi Zhou, Zhibin Yao, Lei Hu

Key Laboratory of Ministry of Education on Safe Mining of Deep Metal Mines, Northeastern University, Shenyang, 110819, China

ARTICLE INFO

Article history:

Received 5 December 2021

Received in revised form

10 December 2021

Accepted 12 December 2021

Available online 23 December 2021

Keywords:

Spalling

Deep cracking

Large deformation

Rockbursts

Excavation-induced deep hard rock

fracturing

Cracking-restraint method

Energy-controlled method

ABSTRACT

To analyze and predict the mechanical behaviors of deep hard rocks, some key issues concerning rock fracturing mechanics for deep hard rock excavations are discussed. First, a series of apparatuses and methods have been developed to test the mechanical properties and fracturing behaviors of hard rocks under high true triaxial stress paths. Evolution mechanisms of stress-induced disasters in deep hard rock excavations, such as spalling, deep cracking, massive roof collapse, large deformation and rockbursts, have been recognized. The analytical theory for the fracturing process of hard rock masses, including the three-dimensional failure criterion, stress-induced mechanical model, fracturing degree index, energy release index and numerical method, has been established. The cracking-restraint method is developed for mitigating or controlling rock spalling, deep cracking and massive collapse of deep hard rocks. An energy-controlled method is also proposed for the prevention of rockbursts. Finally, two typical cases are used to illustrate the application of the proposed methodology in the Baihetan caverns and Bayu tunnels of China.

© 2022 Institute of Rock and Soil Mechanics, Chinese Academy of Sciences. Production and hosting by Elsevier B.V. This is an open access article under the CC BY-NC-ND license (<http://creativecommons.org/licenses/by-nc-nd/4.0/>).

1. Introduction

Increasing numbers of deep hard rock excavations have been or will be conducted in various fields across the world, such as metal mines, traffic tunnels, hydraulic tunnels and powerhouses, oil and gas storage, underground nuclear waste disposal and physics laboratories (Hagan et al., 2001; Hajiabdolmajid and Kaiser, 2003; Xie et al., 2015; Fan et al., 2017; Hatzor et al., 2017; Feng et al., 2018a; Qian and Zhou, 2018). The deep hard rock excavations are basically characterized by high strength (i.e. uniaxial compressive strength (UCS) larger than 60 MPa), high triaxial stress conditions (i.e. depth larger than 1000 m or maximum principal stress $\sigma_1 \geq 20$ MPa), intensive unloading and stress path change induced by massive excavation. These can generally induce various fracturing disasters of hard rocks, such as rockburst (Williams et al., 1992; Ortlepp and Stacey, 1994; Durrheim et al., 1998; Ortlepp, 2005; Feng, 2017), rock spalling (Martin and Christiansson, 2009; Feng et al., 2018a), large deformation (Lin, 1983; Aydan et al., 1993; Hoek and Guevara, 2009; Mercier-Langevin and Hadjigeorgiou, 2013; Liu et al., 2017),

deep cracking (Feng et al., 2017; Qian and Zhou, 2018), and massive collapse (Rajmeny et al., 2002; Li et al., 2009). Long-term fracturing and stability of hard rock masses are also important issues for practical applications (Kusui et al., 2016; Qian and Lin, 2016).

These disasters give rise to significant challenges in underground excavation (Rajmeny et al., 2002; Xia et al., 2007; He et al., 2010; Miranda et al., 2011; Feng and Hudson, 2011; Langford and Diederichs, 2015; Barton and Shen, 2017). For example, the observed stress-induced ejection velocity of rock slices is more than 2.5 m/s in deep gold mining in South Africa (Milev et al., 2001). New cracks inside surrounding rocks in an underground cavern were recorded at 13 m depth, which resulted in long-term reinforcement of more than half a year in the Jinping I underground cavern, China (Song et al., 2016). High stress-induced fracturing and collapse have resulted in a rapid increase in risk level and associated high supporting cost in Jinping underground laboratory phase II (CJPL-II) of China (Feng et al., 2018a). Therefore, a good understanding of the high stress-induced fracturing of deep hard rocks is helpful for optimized excavation and support design and disaster prevention in deep hard rock engineering.

To understand the failure mechanism of deep hard rocks under high geostress conditions, many experimental methods that can consider true triaxial stresses have been developed (e.g. Chen and Feng, 2006; Haimson, 2006; Tiwari and Rao, 2006;

* Corresponding author.

E-mail address: fengxiating@mail.neu.edu.cn (X.-T. Feng).

Peer review under responsibility of Institute of Rock and Soil Mechanics, Chinese Academy of Sciences.

Kwasniewski, 2007; He et al., 2010; Ingraham, 2012; Li et al., 2015; Feng et al., 2016b; Su et al., 2018; Luke et al., 2019). Associated theoretical analysis methods considering the brittle failure of hard rocks have been presented (e.g. Hajiabdolmaji et al., 2002; Rajmeny et al., 2002; Read, 2004; Su et al., 2006; He and Qian, 2010; Qian and Zhou, 2011; Hamdi et al., 2017; Wang et al., 2017; Vazaios et al., 2019; Xie, 2021; Faradonbeh et al., 2022). Energy-absorbing rockbolts and associated support design methods have been developed (e.g. Trinh and Jonsson, 2013; Li, 2017; Louchnikov et al., 2017; Malan and Napier, 2018; Kaiser and Moss, 2021). Advances in the deformation and failure of deep hard rocks obviously enrich our knowledge. However, some key issues must be addressed:

- (1) What are the short- and long-term properties of hard rocks under high true stress conditions ($\sigma_1 > \sigma_2 > \sigma_3$, where σ_2 and σ_3 are the intermediate and minimum principal stresses, respectively)?
- (2) Excavation can change the magnitude and direction of three principal stresses. How do the properties (brittleness and ductility) of hard rock masses change under high stresses during excavation? How do the stress paths affect the properties of hard rock masses?
- (3) What are the behaviors of stiff joints under high true triaxial stresses in the short and long terms? To what extent can joints affect the properties of rock masses under high true triaxial stresses?
- (4) What theory should be developed for analyses of fracturing and deformation behaviors of hard rock masses under high true triaxial stress conditions?
- (5) What are the evolution processes of rock spalling, deep cracking, massive collapse, large deformation and rockbursts?

- (6) What are the effective methods and principles that can be used to mitigate or control rock spalling, deep cracking, massive collapse, large deformation and rockbursts?

To answer these questions, a methodology for excavation-induced fracturing of deep rocks, including rock testing methods and apparatuses, computational analytical theory, and disaster control principles, is proposed in this paper. Two typical case examples are illustrated to show the applicability of these methods and techniques.

2. Methodology of deep hard rock mechanics

A systematic mapping is proposed for studying deep hard rock mechanics, as shown in Fig. 1. In terms of mechanical behaviors, the excavation-induced fracturing of deep hard rocks is focused. It starts in deep geological environments, such as high three-dimensional (3D) geostresses, complex geological structures and large-scale excavations, and typical disasters induced by deep hard rock excavation, such as rock spalling, deep cracking, zonal disintegration, massive collapse, large deformation and rockbursts. The following items are basically required:

- (1) Methods and apparatus for testing the mechanical properties of deep hard rocks under true triaxial stresses and excavation-induced true triaxial stress paths in consideration of the effects of stiff joints, time-dependent behaviors, and excavation disturbance;
- (2) In situ observation method for fracturing, deformation and energy concentration and release process of deep hard surrounding rocks;
- (3) Stress-induced fracturing and deformation behaviors of deep hard rocks, including brittle and ductile characteristics, 3D

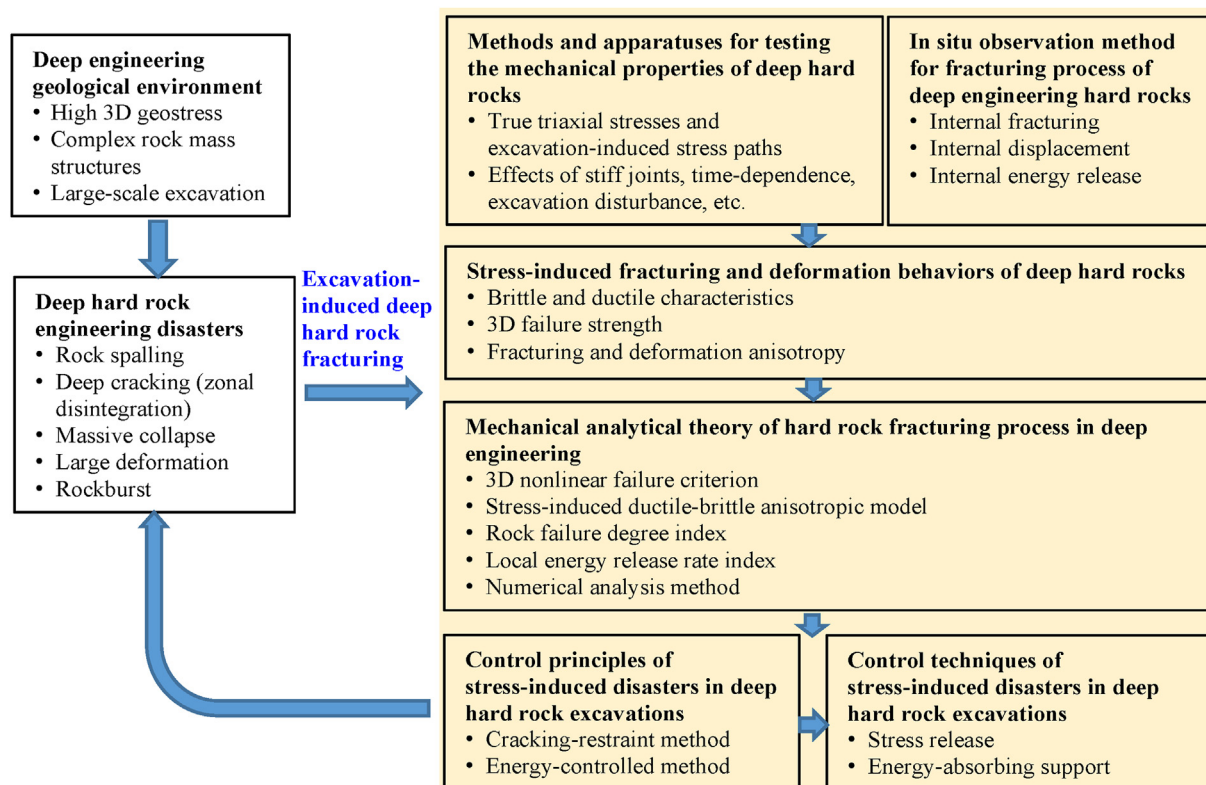


Fig. 1. Systematic mapping of deep hard rock mechanics.

failure strength, fracturing and deformation anisotropy induced by high true triaxial stresses and paths, which result in high stress-induced disasters of deep hard rocks;

- (4) Mechanical analytical theory of the hard rock fracturing process in deep engineering, including the 3D nonlinear failure criterion, stress-induced ductile-brittle anisotropic model, rock failure degree index, local energy release rate (LERR) index, and numerical method;
- (5) Control principles of stress-induced disasters in deep hard rock excavations, including crack-resisting methods for controlling stress-induced disasters such as rock spalling, deep cracking, zonal disintegration, large deformation and massive collapse and energy-controlled methods for controlling rockbursts; and
- (6) Control techniques of stress-induced disasters in deep hard rock excavations, including stress release and energy-absorbing support.

3. Methods and apparatus for testing the mechanical properties of deep hard rocks

As shown in Fig. 2, deep hard rocks suffer naturally high true triaxial stresses ($\sigma_1 > \sigma_2 > \sigma_3$). Furthermore, excavation will induce changes in the triaxial stresses, such as unloading and loading of principal stresses and rotation of principal stress orientation, which result in a complex stress path. After excavation, deep surrounding rocks will suffer a long-term effect of high true triaxial stresses. Blasting, rockbursting and earthquakes would result in stress disturbance on deep hard rocks. These factors will affect the mechanical properties of deep hard rocks. To understand these scenarios, a series of true triaxial apparatuses and in situ observation methods for hard rocks was developed at Northeastern University, China (Table 1). Accordingly, a number of International Society for Rock Mechanics and Rock Engineering (ISRM) suggested methods and Chinese Society for Rock Mechanics and Engineering standards were also proposed (Feng et al., 2019a, 2021a).

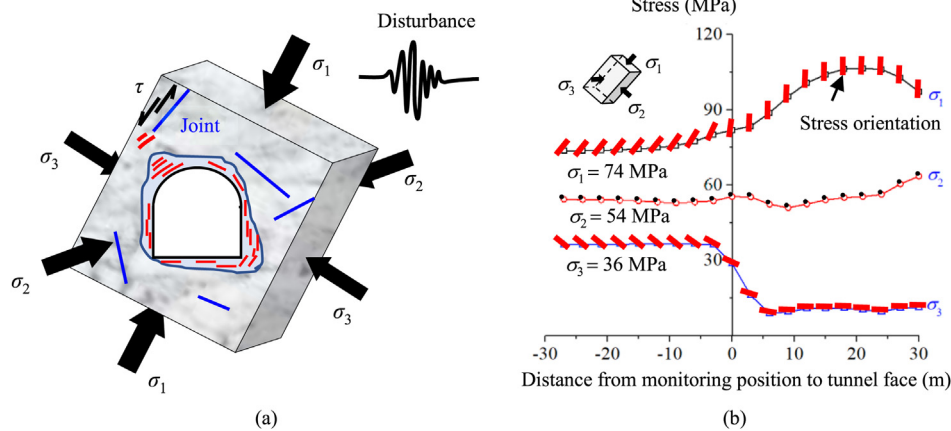


Fig. 2. True triaxial stress characteristics of deep hard rock excavation: (a) True triaxial stress ($\sigma_1 > \sigma_2 > \sigma_3$), and (b) A typical stress path evolution during excavation of deep rock masses.

Table 1

A series of true triaxial testing apparatuses for deep hard rocks.

Type of apparatus	Loading schematic diagram	Feature
True triaxial compression stress path testing apparatus		Complete stress-strain process test; Loading-unloading stress path test; Stress direction transformation test
True triaxial rheology testing apparatus		True triaxial creep test; True triaxial relaxation test
True triaxial shear testing apparatus		True triaxial shear test of stiff joints
True triaxial dynamic disturbance testing apparatus		Low-amplitude disturbance with high frequency in σ_1 direction; Low-amplitude disturbance with low frequency in σ_2 or σ_3 direction

Note: σ_n is the normal stress, σ_p is the lateral stress, F_t is the shear force, and σ_d is the disturbance stress.

3.1. Method and apparatus for testing the mechanical properties of hard rocks under high true triaxial stress paths

A testing apparatus that can consider the true triaxial compression stress path was developed to capture the complete stress-strain curve of hard rocks under high true triaxial stress paths, as shown in Fig. 3. The techniques of the adaptive coordinated feedback control of the rock brittle fracturing process, sliding frame loading, fixing the

specimen center, full-face loading, and friction reduction of the rock sample surface, acoustic emission (AE) sensors attached to the rock sample, and three-axial displacement meters were developed to obtain accurate testing results. By using this apparatus, the strength, brittle and ductile properties, complete stress-strain curves, AE events and fracturing process of hard rocks under true triaxial compression paths were obtained, as shown in Fig. 4.



Parameter	Value
Horizontal force	0–3000 kN
Vertical force	0–6000 kN
Cell pressure	0–100 MPa
Stiffness	6 GN/m
Deformation measuring accuracy	0.1 μm
Feedback control accuracy	0.2 ms
AE sensor's bearing capacity	0–100 MPa
Friction coefficient	0.02

Fig. 3. True triaxial compression stress path testing apparatus for obtaining the complete stress-strain curve of deep hard rocks under high true triaxial stress paths (Feng et al., 2016a).

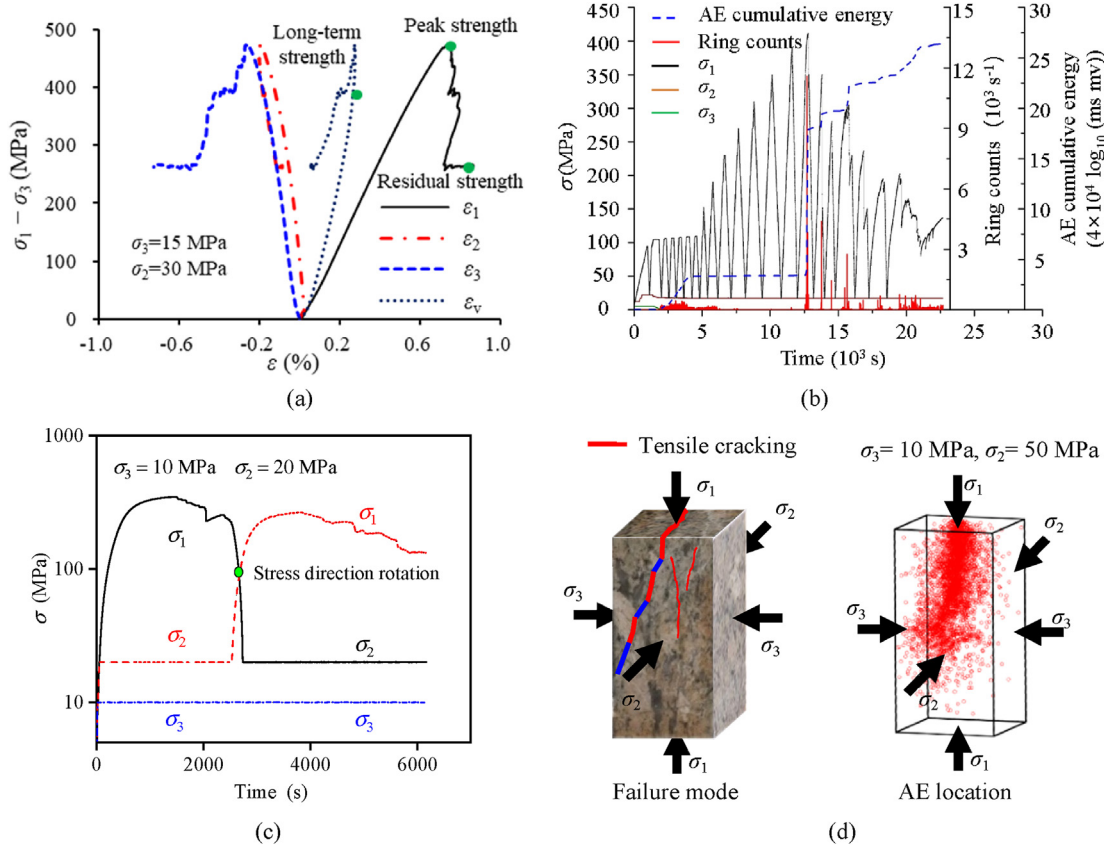
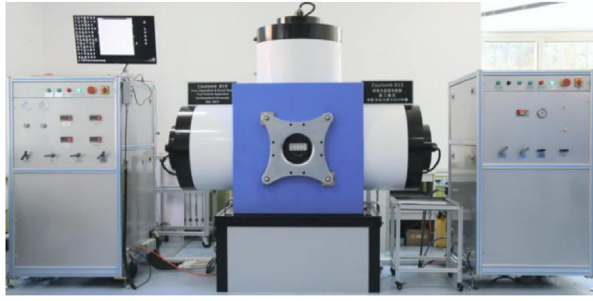


Fig. 4. Typical testing results of hard rocks under the true triaxial compression stress path: (a) Complete stress-strain curves of basalt at the Baihetan hydropower station of China under true triaxial stress compression (ϵ_1 , ϵ_2 and ϵ_3 are the strains in the σ_1 , σ_2 and σ_3 directions, respectively); (b) AE results of Sweden Forsmark granite under complex σ_1 loading-unloading, loading-unloading and stable σ_2 and σ_3 ; (c) Stress vs. time curves of Portugal granite under transformation of σ_1 and σ_2 at the post-peak stage and stable σ_3 ; and (d) Stress-induced tensile and shear cracking and associated AE results of altered granite from the Sanshandao gold mine of China.



Parameter	Value
Horizontal force	0–3000 kN
Vertical force	0–6000 kN
Cell pressure	0–100 MPa
Stiffness	16 GN/m
Eccentricity	2 μm
Holding time with constant stress	180 d

Fig. 5. True triaxial rheology testing apparatus for deep hard rocks under high true triaxial stresses (Feng et al., 2018b).

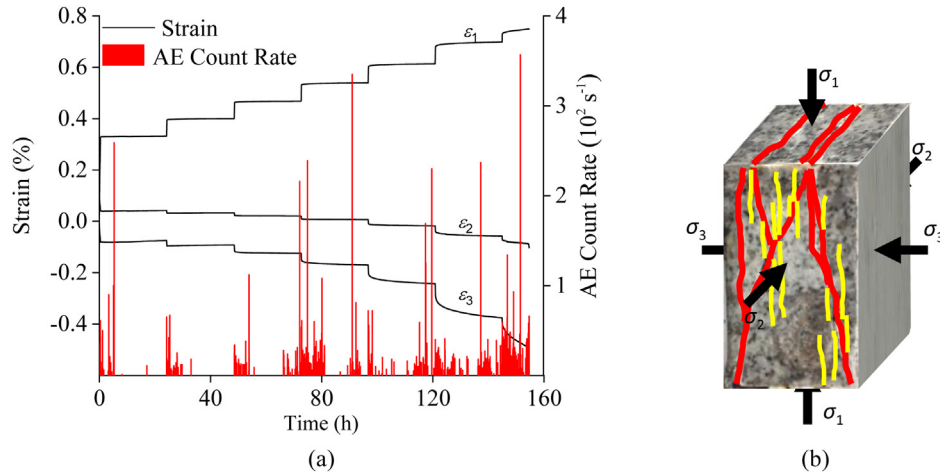


Fig. 6. Typical true triaxial pre-peak creep test results of granite at the Bayu tunnel under $\sigma_3 = 5$ MPa and $\sigma_2 = 30$ MPa: (a) True triaxial stress-induced anisotropic time-dependent fracturing and deformation, and (b) Final failure planes (red lines) caused by a series of tensile fracture (yellow lines) groups (Zhao et al., 2021a).

3.2. Method and apparatus for testing the rheological properties of hard rocks under true triaxial compression

A true triaxial rheology testing apparatus was developed to study the time-dependent failure process of hard rocks under high triaxial stresses, as shown in Fig. 5. The techniques of a super rigid frame, fixing the specimen center, full-face loading, and friction reduction of the rock sample surface, AE sensors attached to the rock sample, and three-axial displacement meters were developed to obtain accurate results. By using this apparatus, the full creep and relaxation process of hard rocks accompanied by AE events at

both pre-peak and post-peak under true triaxial compression can be obtained, as shown in Figs. 6 and 7, respectively.

3.3. Method and apparatus for testing the shear behavior of hard rocks under true triaxial compression

To understand the shear behaviors of stiff joints in deep hard rocks, a true triaxial shear box was developed, as shown in Fig. 8. The shear box needs to be assembled into the above-mentioned true triaxial apparatus to perform a single-shear test under true triaxial compression. Complete shear stress-displacement curves in

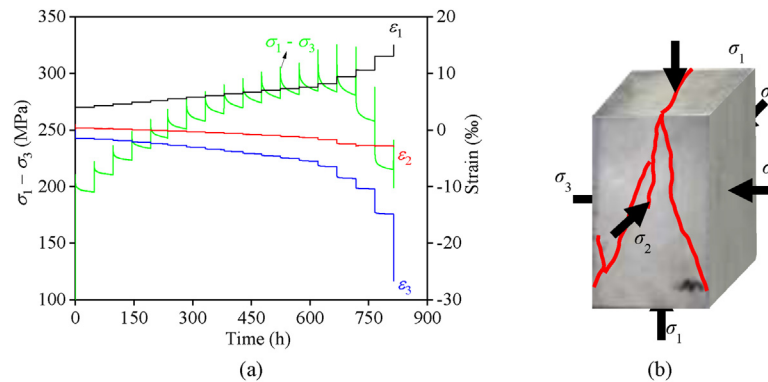
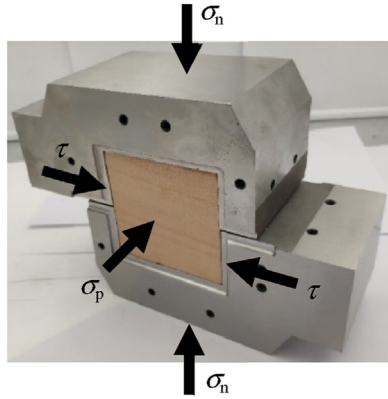


Fig. 7. Typical true triaxial relaxation test results of CJPL-II marble under $\sigma_3 = 20$ MPa and $\sigma_2 = 50$ MPa: (a) Difference in lateral time-dependent deformation, and (b) Final failure planes (failure surface nearly parallel to the σ_2 direction and open along the σ_3 direction) (Zhao et al., 2021b).



Parameter	Value
Shear force	0–3000 kN
Normal force	0–6000 kN
Cell pressure	0–100 MPa
Deformation measurement range	0–3 mm
Deformation measurement accuracy	0.1 μm
Friction coefficient	0.02

Fig. 8. Shear box assembled into a true triaxial compression apparatus to carry out true triaxial single-shear tests of cubic rock samples (Feng et al., 2021b).

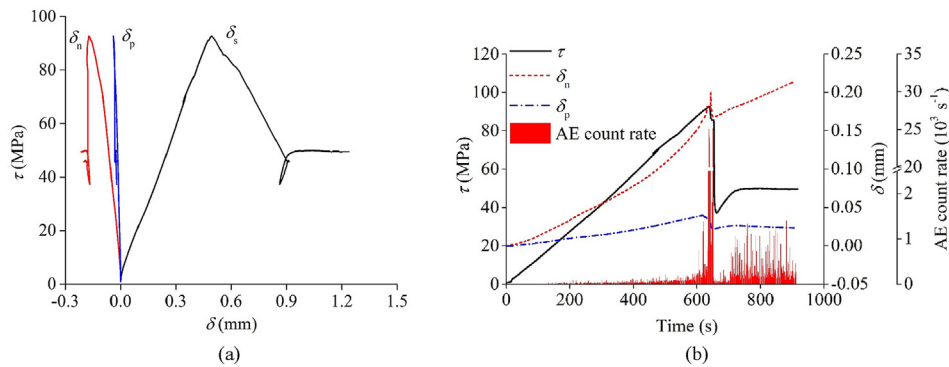


Fig. 9. Typical true triaxial single-shear testing results of jointed granite at the Bayu tunnel under $\sigma_n = 50$ MPa and $\sigma_p = 20$ MPa: (a) Complete shear stress-deformation curves in the normal, shear and lateral directions; and (b) Evolution of the AE count rate.

three directions can be obtained (Fig. 9a) to study the failure evolution mechanism, and the fracturing process is recorded by the AE technique (Fig. 9b).

3.4. Method and apparatus for testing the dynamic behaviors of hard rocks under true triaxial compression

To understand the failure mechanism of deep hard rocks induced by excavation disturbances, a novel true triaxial system with dynamic disturbance was developed (Fig. 10). High-frequency and low-amplitude disturbances and low-frequency and low-amplitude disturbances of hard rocks at both pre-peak and post-

peak that are applied in the σ_1 direction (Fig. 11) and in the σ_2 or σ_3 direction (Fig. 12), respectively, are realized to study the blasting vibration effect.

3.5. In situ observation method for the disaster development process

In situ observation of the deep hard rock excavation process is conducted by multiple monitoring means, such as digital borehole cameras, acoustic wave testing, displacement meters and sliding micrometers, AE techniques (Feng et al., 2019b), and microseismic monitoring (Xiao et al., 2016), to directly and continuously record



Parameter	Value
X-axial static force	0–2000 kN
Y-axial static force	0–3000 kN
Z-axial static force	0–2000 kN
Z-axial frequency and amplitude	0–20 Hz, 0–30 MPa
X-axial frequency and amplitude	100–500 Hz, 0–30 MPa
Stiffness	20 GN/m
Deformation measuring accuracy	0.1 μm
Feedback control accuracy	0.1 ms

Fig. 10. True triaxial dynamic disturbance apparatus for deep hard rocks under high true triaxial stresses.

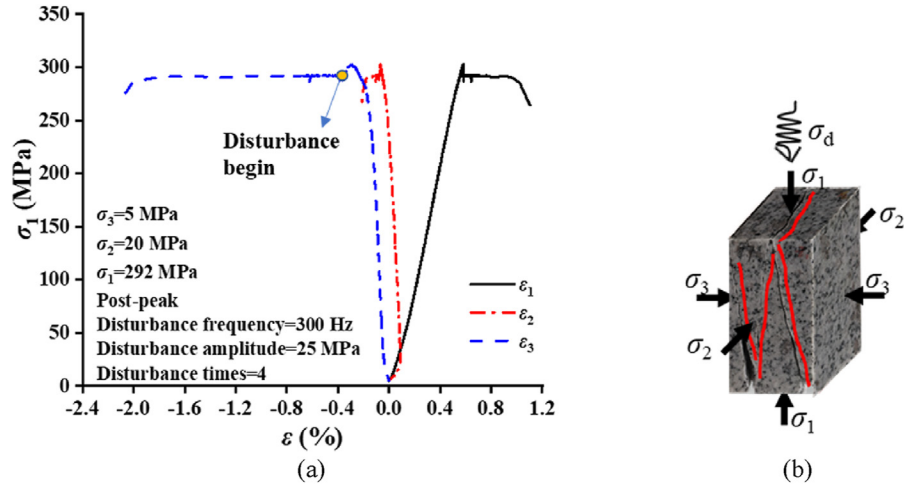


Fig. 11. Testing results of the true triaxial compression of Bayu tunnel granite disturbed by high-frequency and low-amplitude disturbance loads from the σ_1 direction at the post-peak stage: (a) Complete stress-strain curves, and (b) Macroscopic shear failure mode.

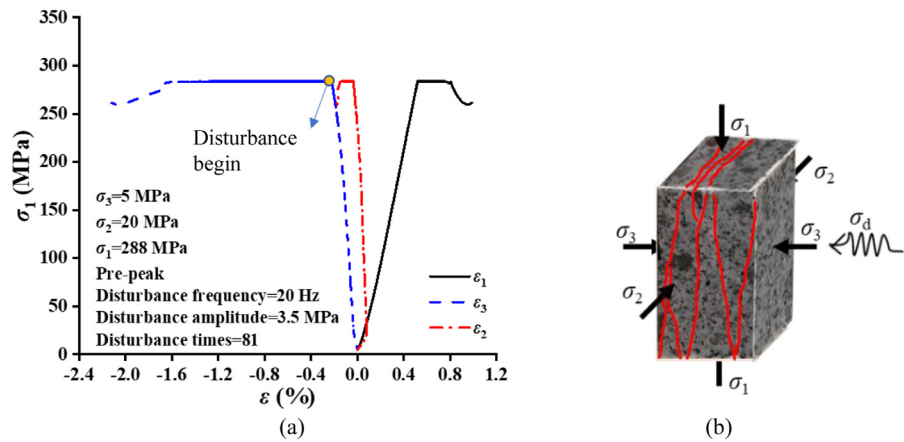


Fig. 12. Results of the true triaxial compression tests on Bayu tunnel granite disturbed by low-frequency and low-amplitude disturbance loads from the σ_3 direction at the pre-peak stage: (a) Complete stress-strain curves, and (b) Splitting failure induced by tensile cracking.

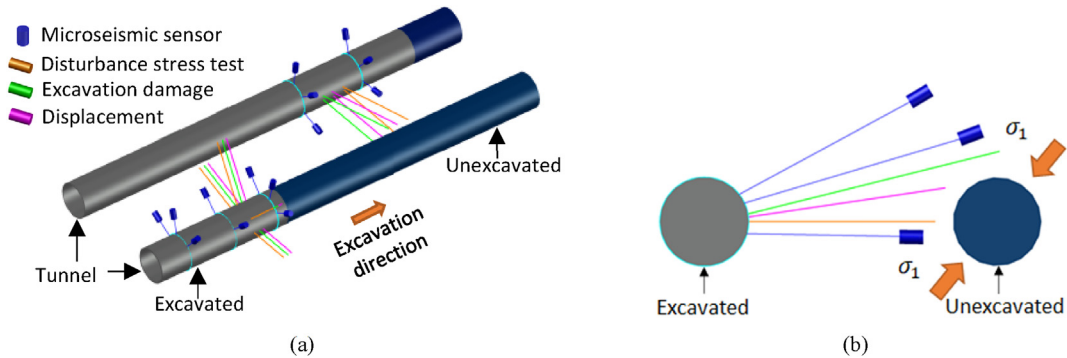


Fig. 13. In situ observation of the evolution process of fracturing and deformation of hard surrounding rocks in deep excavations: (a) Observation layout and (b) Geometrically asymmetric arrangement of observations according to the estimated positions with high disaster risk or significant surrounding rock response.

multiple responses of surrounding rocks, including fracturing, damaging, deformation and energy release, as shown in Fig. 13. Regarding the layout of monitoring boreholes, the basic principle is to cover the areas with high disaster risk or significant surrounding rock response and to obtain the whole process of the rock mass mechanical response. First, the rock response of the observation area is evaluated by numerical analysis, geological assessment and

other methods to locate the areas with high disaster risk or significant response. Observation measures are pre-installed in the observation area so that the initial value of the internal characteristics of the rock mass can be obtained before excavation, and these characteristics are continuously tracked and observed during the excavation process to analyze the evolution mechanisms of disasters.

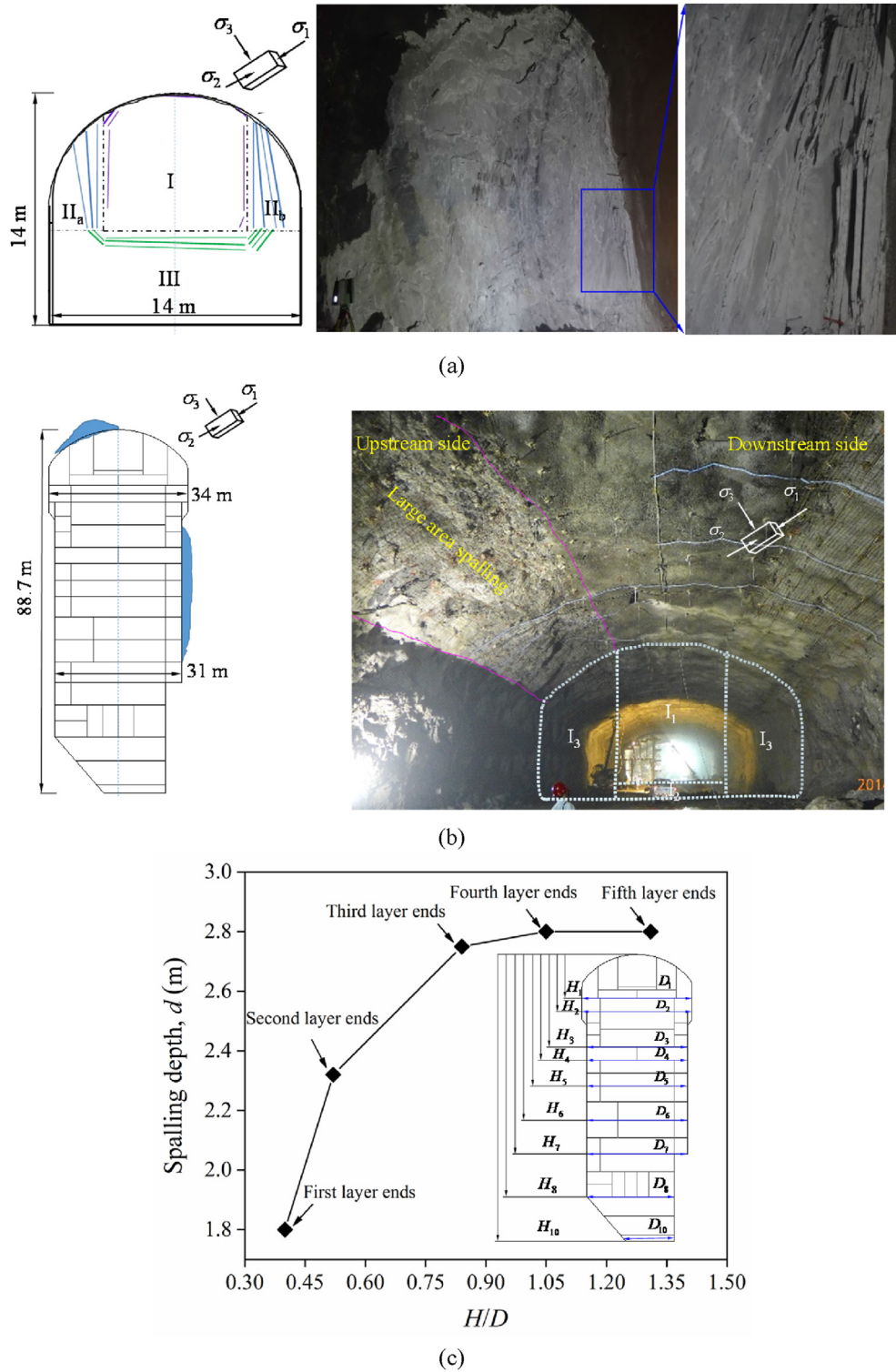


Fig. 14. Typical engineering excavation structures, failure mechanism and modes and site photos of rock spalling during (a) the pilot tunnel excavation of tunnel No. 7 of CJPL-II (after Feng et al., 2018a), (b) the first layer excavation of the underground powerhouse on the left bank of the Baihetan hydropower station (after Liu et al., 2017), and (c) the results of spalling evolution under layered and divisional excavation of a large underground powerhouse.

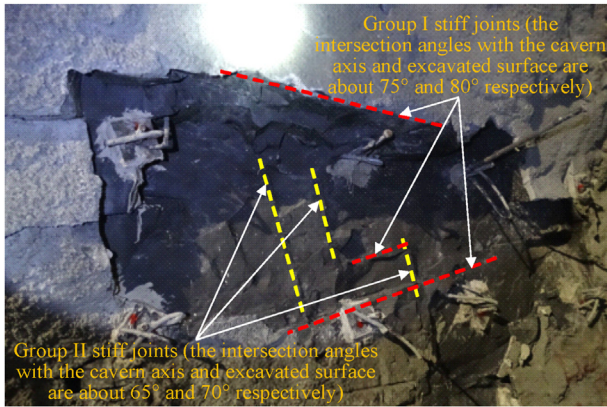


Fig. 15. Influence of stiff joints on the rock spalling of the underground powerhouse at Baihetan hydropower station (Liu et al., 2017).

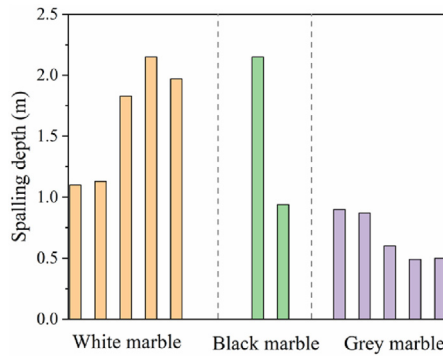


Fig. 16. Relationships between lithology and depth of rock spalling in tunnels Nos. 7 and 8 of CJPL-II (data from Feng et al., 2018a).

4. Evolution mechanisms of stress-induced disasters in deep hard rock excavations

4.1. Evolution mechanism of rock spalling in deep hard rock excavations

Rock spalling is a phenomenon in which flaky or plate-shaped fragments break off from a deep intact or relatively intact hard and brittle rock mass under the action of excavation or other external disturbances. It occurs near the tunnel boundary, and the spalling slabs show tensile fracture approximately parallel to the excavation surface, which is consistent with the tangential stress

direction (Fig. 14a). In addition, the slabs are alternately thick and thin and gradually increase in thickness from the sidewall inwards (Feng et al., 2017). For large underground excavations (Fig. 14b), spalling will not occur continuously along its axis due to the varied lithology of the strata and complex geological structures encountered, but large-scale local spalling can take place (Liu et al., 2017). In addition, layered and divisional excavation of large caverns (increase in height to span ratio) leads to gradual increases in the area and depth of rock spalling (Fig. 14c).

Compared with intact rock, a rock mass containing stiff joints has a lower stress threshold upon spalling. If the stiff joints intersect the tunnel wall at a large angle, such stiff joints can generally constitute the boundary of spalling (Fig. 15). For excavations crossing different lithologies, the difference in crack initiation stress between rocks can lead to a difference in the spalling depth (Fig. 16). Considering the influences of lithology, in situ stress and height to span ratio on spalling depth, an estimation method of rock mass spalling depth has been established as

$$d_s = Ar \frac{f(\sigma_1, \sigma_2, \sigma_3, H/D)}{I_p \sigma_{ci}^{3D}} \quad (1)$$

where d_s is the spalling depth; r is the effective radius of the tunnel or underground cavern; H/D is the height to span ratio, and $H/D \leq 2$, and when $H/D > 2$, it is calculated as 2; A is the coefficient, and $A < 1$; I_p is the crack propagation capacity index; and σ_{ci}^{3D} is the crack initiation stress under true triaxial compression (Han et al., 2021).

4.2. Evolution mechanism of deep cracking in deep hard rock excavations

Deep fracturing refers to fracturing occurring at a certain distance from the boundary of a cavern. It is generally assumed that either the depth involved (d in Fig. 17) is greater than 5–7 m or that the distance from the fracturing location to the periphery of the large cavern is roughly equal to or greater than the length of the rockbolts used (Feng et al., 2017). The deep fracturing of the surrounding rocks mainly has three modes (Fig. 17).

The evolution mechanism of deep cracking can be attributed to the transfer of stress to the deep surrounding rocks during excavation under high geostress, leading to internal fracturing of intact rock or existing stiff joints (Fig. 18). The fracturing depths of the rock mass are mainly affected by the level and orientation of the initial geostress, the excavation size of the cavern and the quality of the rock mass. When fracturing occurs, the displacement increases suddenly, and the crack width is close to the displacement increment (Fig. 19).

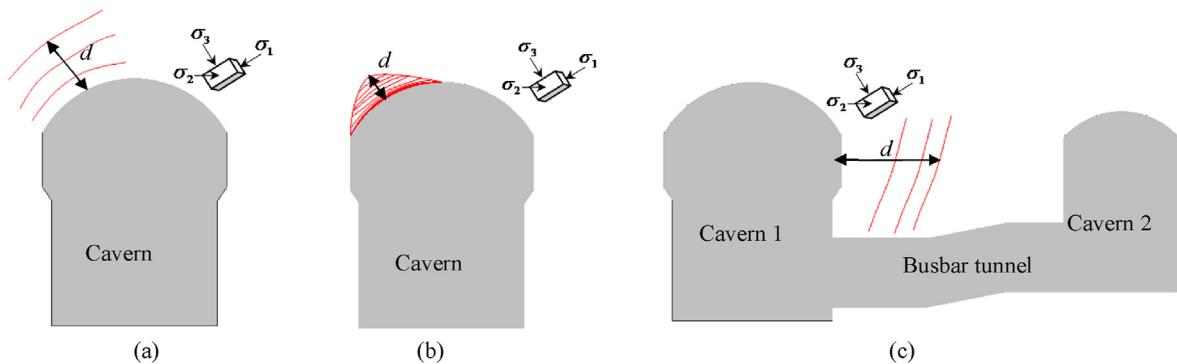


Fig. 17. Schematic diagrams of rock fracturing modes for deep cracking of the surrounding rocks in large underground caverns: (a) Zonal disintegration mainly due to fracturing of the rock mass with discontinuities; (b) Progressive fracturing of the intact rock mass under high stress; and (c) Rock pillar fracturing between two or more caverns.

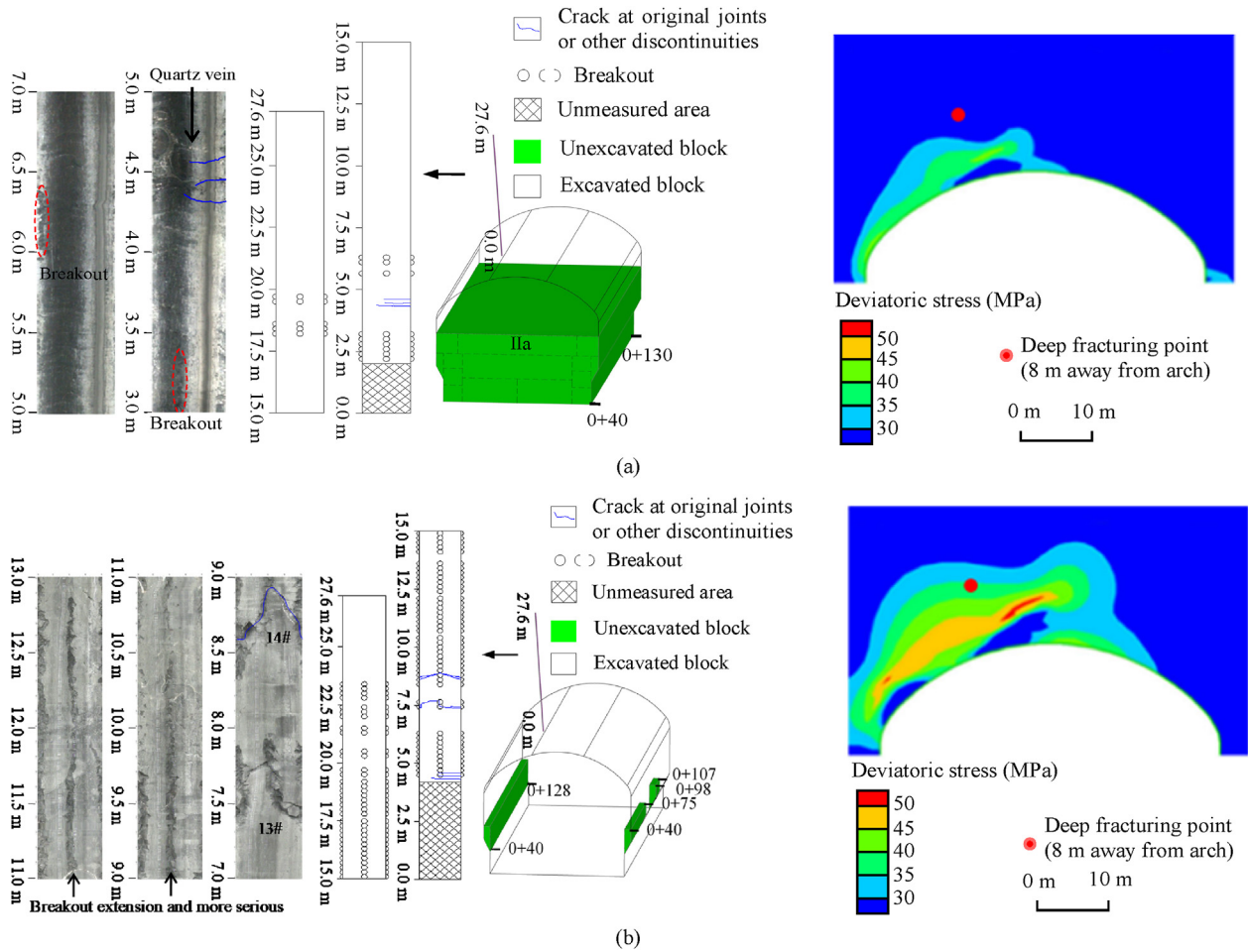


Fig. 18. Evolution of the observed rock fracturing and simulated deviatoric stress in the upstream arch at chainage 0 + 72 of the right bank underground powerhouse of Baihetan hydropower station during downward excavation: (a) Results obtained on December 2, 2014 (excavation of layer I), and (b) Results obtained on November 29, 2015 (excavation of layer III).

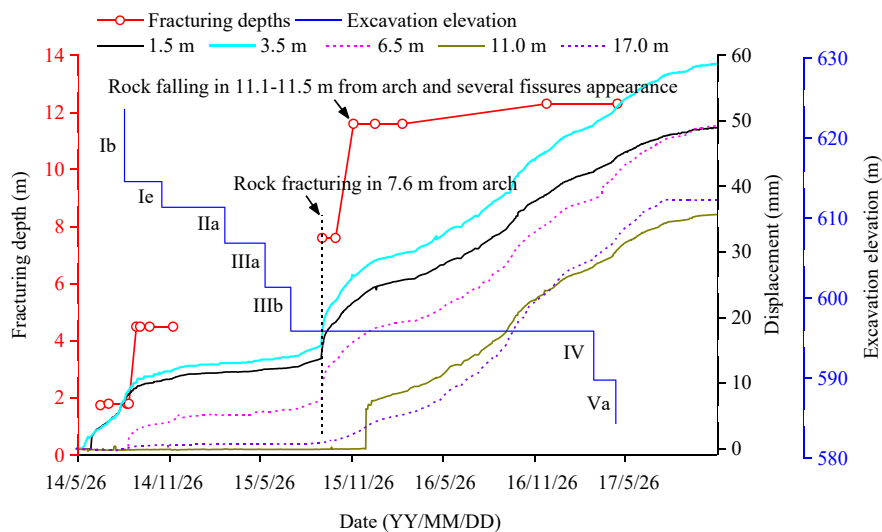


Fig. 19. Evolution of the cracking depths and displacements at different distances from the boundary of the right bank underground powerhouse of the Baihetan hydropower station in the crown arch at chainage 0 + 076 with time as excavation progresses.

4.3. Evolution mechanism of collapse in deep hard rock excavations

The evolution mechanism and characteristics of collapse in deep hard rock excavations can be summarized as follows:

- (1) The collapse is typically stress and structurally controlled. This occurs due to the combination of internal cracking evolution of deep hard rocks and activities of existing geological structures such as weak interlayer zones (WIZs),

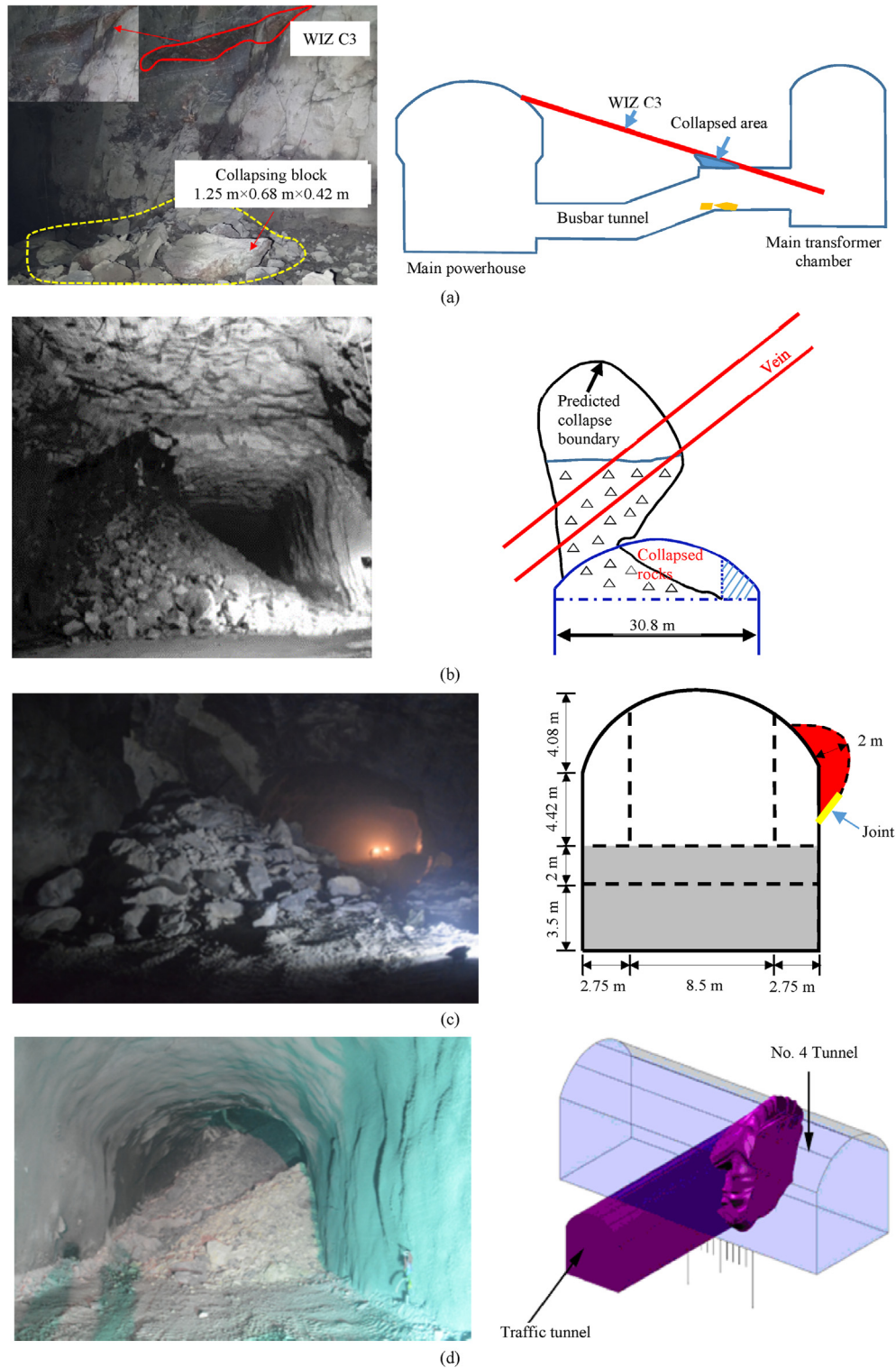


Fig. 20. Typical stress and structurally controlled collapse mode in deep hard rock excavations: (a) Busbar tunnel of Baihetan hydropower station (Zhao et al., 2018); (b) Underground powerhouse of Dagangshan hydropower station (Zhang, 2010); (c) Tunnel No. 4 of CJPL-II; and (d) Tunnel No. 3 of CJPL-II.

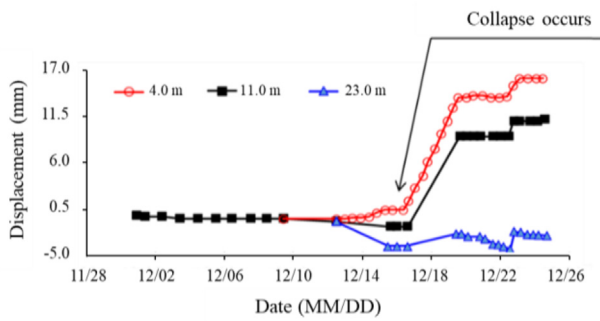


Fig. 21. Measured displacement at different depths in the surrounding rocks during a large-volume collapse in the underground powerhouse of the Dagangshan hydro-power station (Zhang, 2010).

faults, shear zones, veins and joints. The collapse boundary is basically composed of pre-existing discontinuities and newly developed cracks (Fig. 20);

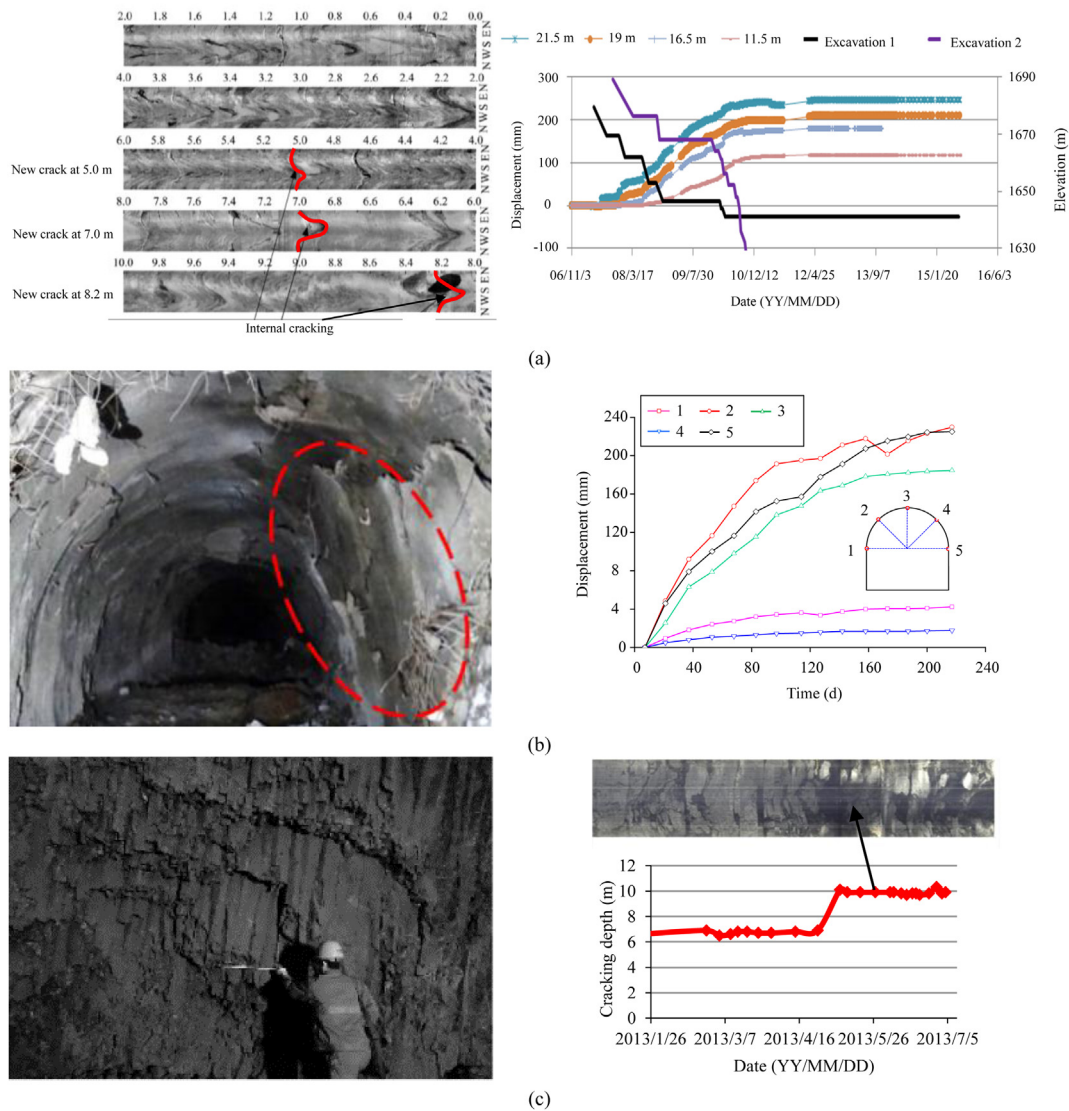


Fig. 22. Typical large deformation problems in deep hard rock engineering: (a) Large deformation (over 200 mm) and internal cracking in the Jinping I powerhouse (Li et al., 2009; Lu et al., 2010); (b) Large deformation (over 200 mm) and internal cracking in the deep roadway of the Jinchuan nickel mine; and (c) Cracking and relaxation (over 10 m) of columnar jointed basalt in the Baihetan diversion tunnel (Wang et al., 2017).

- (2) It usually exhibits a large volume and results in large blocks, e.g. the total volume of collapsed rocks in the Dagangshan powerhouse (Fig. 20b) is over 3500 m³ (Zhang, 2010), and the collapsed block in tunnel No. 4 of CJPL-II is up to 0.2 m × 0.5 m × 0.7 m in size (Fig. 20c);
- (3) Only small deformation occurs before collapse occurrence (Fig. 21).

4.4. Evolution mechanism of large deformation in deep hard rock excavations

The characteristics of large deformation in deep hard rock excavations can be summarized as follows:

- (1) The large deformation of deep hard surrounding rocks is mainly dependent on the high stress-induced internal fracturing of intact rock or existing joints, with the increases in internal cracking depth and degree over time after excavation, as shown in Figs. 22a, c and 23;

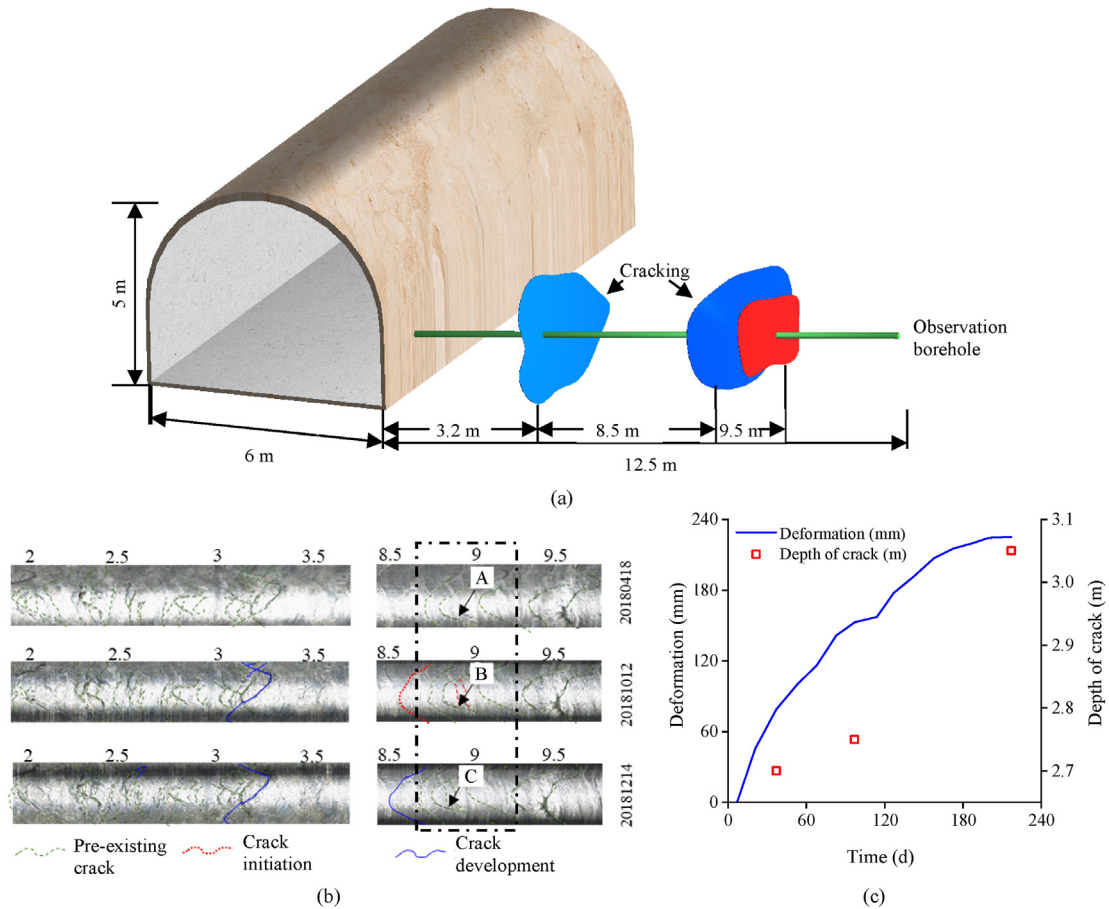


Fig. 23. Continuous observations of the cracking process within the cataclastic rocks in the deep roadway of the Jinchuan nickel mine: (a) Sketch of the observation layout; (b) A newly developed crack at a depth of 9 m growing gradually from 7.2 mm in width (position A) to 8.4 mm (position B) and 9.4 mm (position C) over time; and (c) Relationship between the surface deformation and maximum cracking depth.

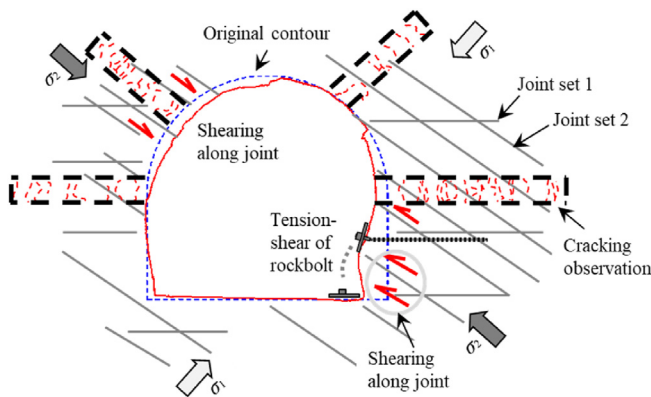


Fig. 24. Evolution mechanism of the large deformation in cataclastic hard rocks in deep roadway of Jinchuan nickel mine.

- (2) The deformation of the surrounding rocks is asymmetric and time-dependent. Fig. 22b shows an asymmetric failure of a deep mine roadway after 7 months of excavation and asymmetric time-dependent convergence; and
- (3) The convergence grows synchronously with the internal cracking. As seen in Fig. 23, both the cracking depth and convergence increase with elapsed time.

For deep cataclastic hard rocks, excavation unloading causes the loosening and opening of tightly compressed internal structures, and the tunnel surface can then exhibit bulking due to the loosening of blocks and joints. The stress-concentration zone then shifts toward the internal intact rock mass. If this internal cracking is not controlled in time, the cracking depth increases over time, and finally, deep fracturing occurs. In summary, the stress-induced asymmetrical development of internal cracking causes asymmetrical deformation, while the time-dependent development of internal cracking induces time-dependent deformation. Continuous cracking within the cataclastic hard rocks results in severe floor heave and unacceptably large deformation of tunnel walls, which eventually leads to a completely failed tunnel under the continuous bulking of the rock mass (Fig. 24).

4.5. Evolution mechanism of rockburst in deep hard rock excavations

Rockburst is a sudden release of elastic potential energy of deformation accumulated in engineering rock masses under excavation or other disturbances, which results in the dynamic phenomenon of violent failure and ejection of surrounding rocks (Feng et al., 2019c; Hu et al., 2020). According to the rockburst mechanism, rockbursts can be divided into strainbursts, strain-structure slip rockbursts and fault slip rockbursts. As shown in Fig. 25, strainburst mainly occurs in hard, intact rock masses without structural planes. The development process of strainburst mainly includes the initiation, propagation and coalescence of new

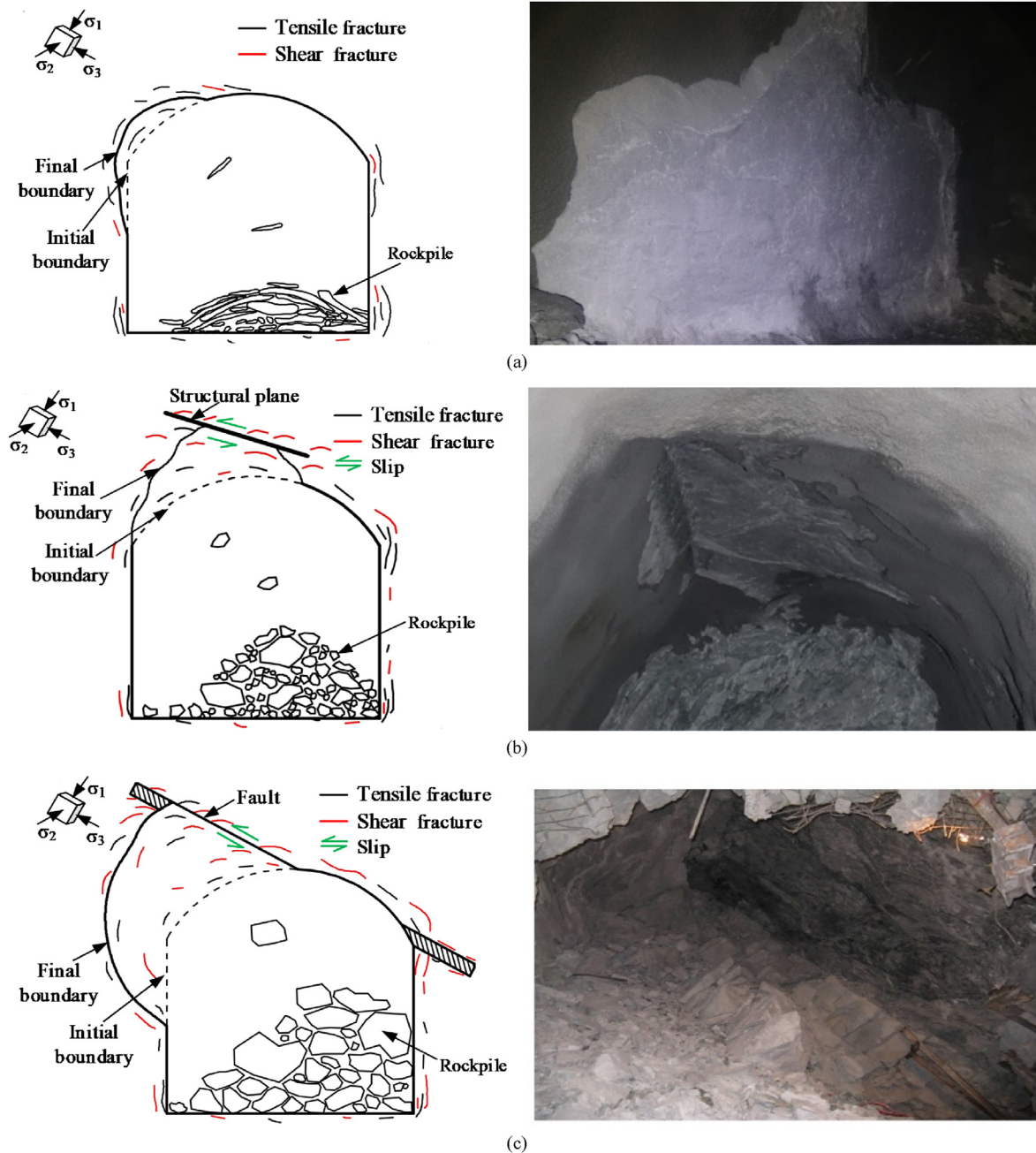


Fig. 25. Typical failure modes and site photos of different types of rockbursts: (a) Strainburst, (b) Strain-structure slip rockburst, and (c) Fault slip rockburst.

fractures and the ejection of bursting bodies. Strain-structure slip rockburst mainly occurs in hard rock masses with a few structural planes that slip during the development process of rockburst. Fault slip rockburst mainly occurs near large-scale faults, and its formation mechanism is not completely clear. One view is that fault slip rockburst is mainly produced by the large amount of energy released by fault slip. Generally, fault slip rockburst has the largest damage scale, followed by strain-structure slip rockburst, and strainburst is the smallest.

As shown in Fig. 26a, fractures generated during the development process of strainburst are basically tensile, and they closely follow the working face as it moves forward. During the development process of strain-structure slip rockburst, the proportion of shear fractures is larger than that of strainburst fractures, and the

fractures are still close to the rockburst area as the working face moves forward (Fig. 26b).

As shown in Fig. 27, the time-history curves of the microseismicity during the development process of immediate rockburst, time-delayed rockburst and intermittent rockburst are different. For immediate rockburst, the number of microseismic events and the microseismic energy are constantly increasing, and there is a sudden increasing trend before rockburst. For time-delayed rockburst, there is an obvious calm period in terms of microseismicity. For intermittent rockburst, the microseismicity fluctuates, and the microseismic energy is released gradually.

Rockburst may occur at any part of the tunnel cross-section. The position of rockburst with respect to the tunnel cross-section is mainly related to the spatial relationship between the structural

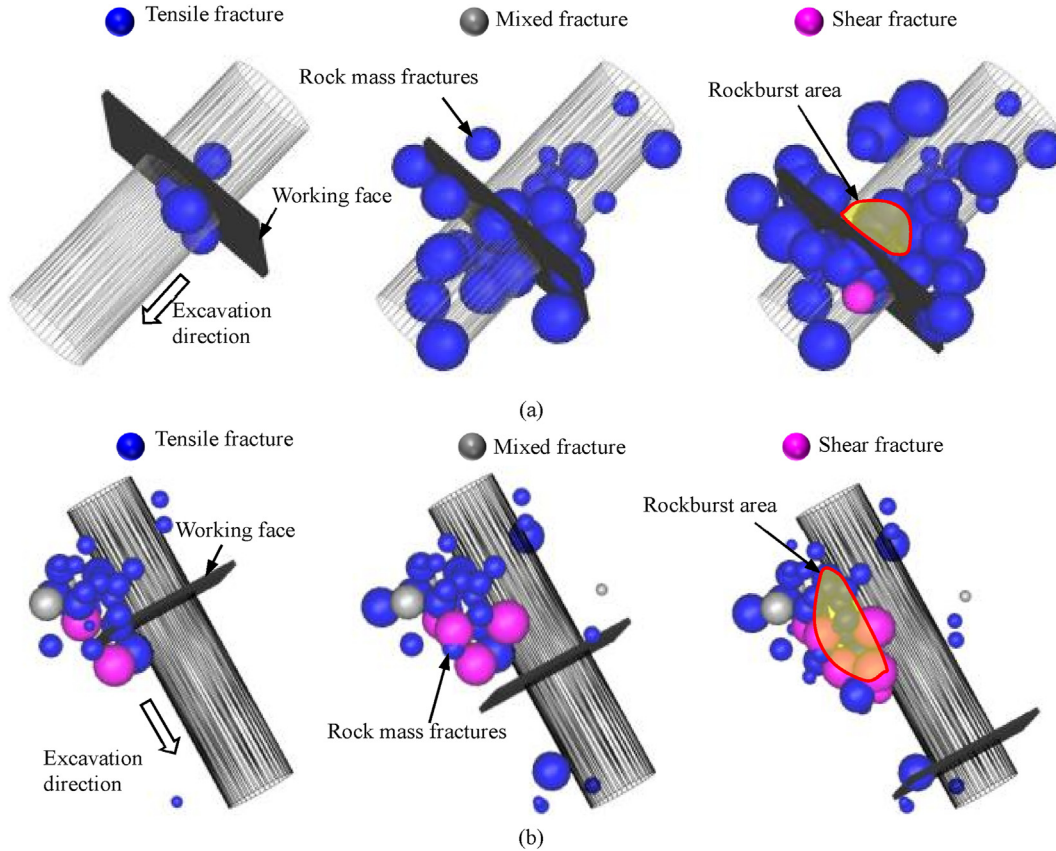


Fig. 26. Typical evolution characteristics of rock mass microfractures around the rockburst area during the development process of rockburst occurred in the Jinping II hydropower station ($\sigma_1 = 63$ MPa, $\sigma_2 = 34$ MPa, $\sigma_3 = 26$ MPa): (a) A strainburst occurred on August 18, 2010 in a tunnel boring machine (TBM) tunnel, and (b) A strain-structure slip rockburst occurred on November 20, 2011 in a tunnel excavated using the drill-and-blast method.

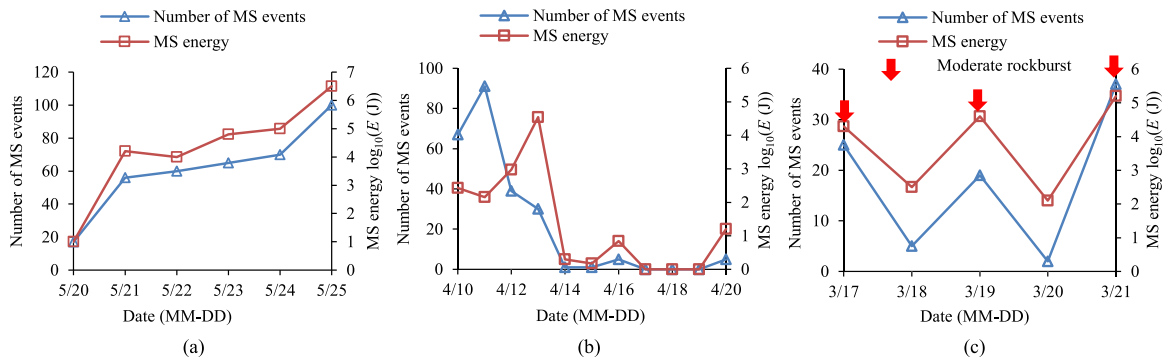


Fig. 27. Typical time-history curves of microseismicity for different types of rockbursts: (a) Immediate rockburst, (b) Time-delayed rockburst, and (c) Intermittent rockburst. MS represents the 'microseismic'.

plane and the maximum principal stress (Hu et al., 2020). Taking a railway tunnel as shown in Fig. 28 as an example, when the direction of the maximum principal stress intersects the structural planes at a large angle in the tunnel cross-section, relative sliding of the rock mass along the structural planes rarely occurs, and rockburst always occurs near the cross-sectional boundary that intersects the direction of the maximum principal stress at a large angle. When the direction of the maximum principal stress intersects the structural planes at a low angle in the tunnel cross-section, relative sliding of the rock mass along the structural planes occurs, and rockburst always occurs near the cross-sectional

boundary that intersects the direction of the maximum principal stress at a low angle.

Rockbursts of different intensities can occur in the same project. For example, during excavation of CJPL-II, slight, moderate, intense and extremely intense rockbursts were observed. Different geological conditions, especially differences in structural plane development, are the main reasons for different rockburst intensities. Generally, low-intensity rockburst is mainly induced by the excavation unloading stress, while high-intensity rockburst is induced by the local concentration of excavation unloading stress and unfavorable structural planes. In addition, less energy

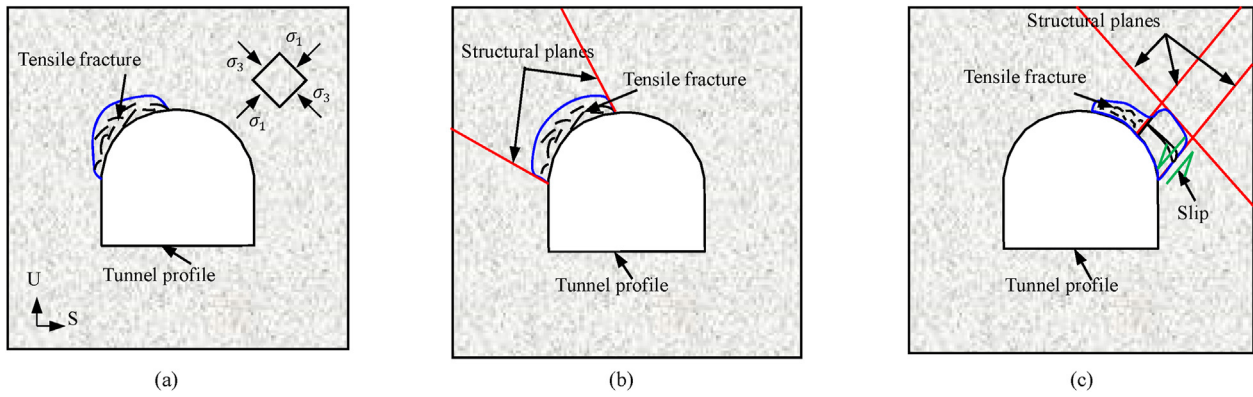


Fig. 28. Schematic diagram of the rockbursts occurred (a) at the north spandrel of the tunnel wherein no clear structural plane was revealed, (b) at the north spandrel of the tunnel wherein two stiff structural planes were revealed, and (c) at the south sidewall to the south spandrel of the tunnel wherein three stiff structural planes were revealed.

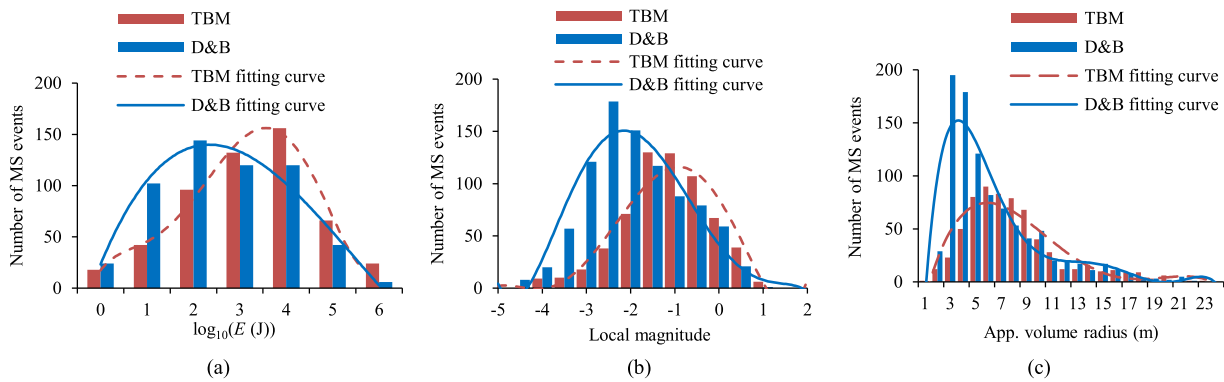


Fig. 29. Characteristics of the microseismicity during the development process of moderate rockburst in tunnels with similar geological conditions and different excavation methods: (a) Magnitude distribution, (b) Energy distribution, and (c) Fracture scale distribution.

accumulates in the rock mass during the development process of low-intensity rockburst, and less energy is released when low-intensity rockburst occurs, while more energy accumulates during the development process of high-intensity rockburst, and more energy is released when high-intensity rockburst occurs.

As shown in Fig. 29, the magnitude, microseismic energy and fracture scale of microseismic events generated during the development process of rockburst in tunnels excavated by the TBM are all larger than those in tunnels excavated by the drill-and-blast method.

5. Stress-induced fracturing and deformation properties of deep hard rocks

5.1. Brittle and ductile failure and deformation characteristics of deep hard rocks

The brittleness and ductility of deep hard rocks are closely related to the post-peak failure and deformation characteristics, referred to as instability failure with and without a sudden decrease in bearing capacity, respectively (Fig. 30a). During brittle failure, tensile crack evolution becomes localized; thus, brittle fracturing occurs readily when cracks are mutually connected after the peak strength is reached, while many uniformly distributed microcracks caused by dislocation glide are found within the rock, and the crack evolution is mainly concentrated on local shear zones to form shear failure surfaces during ductile

failure (Fig. 30b). The brittleness and ductility of deep hard rocks are affected by the 3D stress state (Fig. 30c). That is, a high stress difference ($\sigma_2 - \sigma_3$) increases the brittleness, and the true triaxial stress boundary condition of the brittle-ductile transition of CJPL-II marble can be described as $\sigma_3 - 0.15\sigma_2 = 13$ (Zhao et al., 2018). In addition, the brittleness and ductility of deep hard rocks are affected by rock lithology (Fig. 30d).

5.2. Stress-induced fracturing and deformation anisotropy of deep hard rocks

Stress-induced fracturing anisotropy refers to directional crack propagation. The rock fracture surface appears parallel to the direction of σ_2 (Fig. 4d). The failure mechanism of hard rocks under true triaxial stresses is dominated by tensile cracking, which shows a step-shaped or splitting failure mode (Fig. 4d). The failure angle of the main failure surface is mainly affected by σ_3 , as shown in Fig. 31a. As a result of the fracturing anisotropy, the deformation along different directions also shows stress-induced anisotropy, as shown in Fig. 4a. With increasing stress difference ($\sigma_2 - \sigma_3$), the anisotropy degree increases (Feng et al., 2019d), as shown in Fig. 31b.

5.3. Stress-induced strength characteristics of deep hard rocks

Rock strengths, including peak strength, long-term strength, and residual strength, are related to different stages of the rock

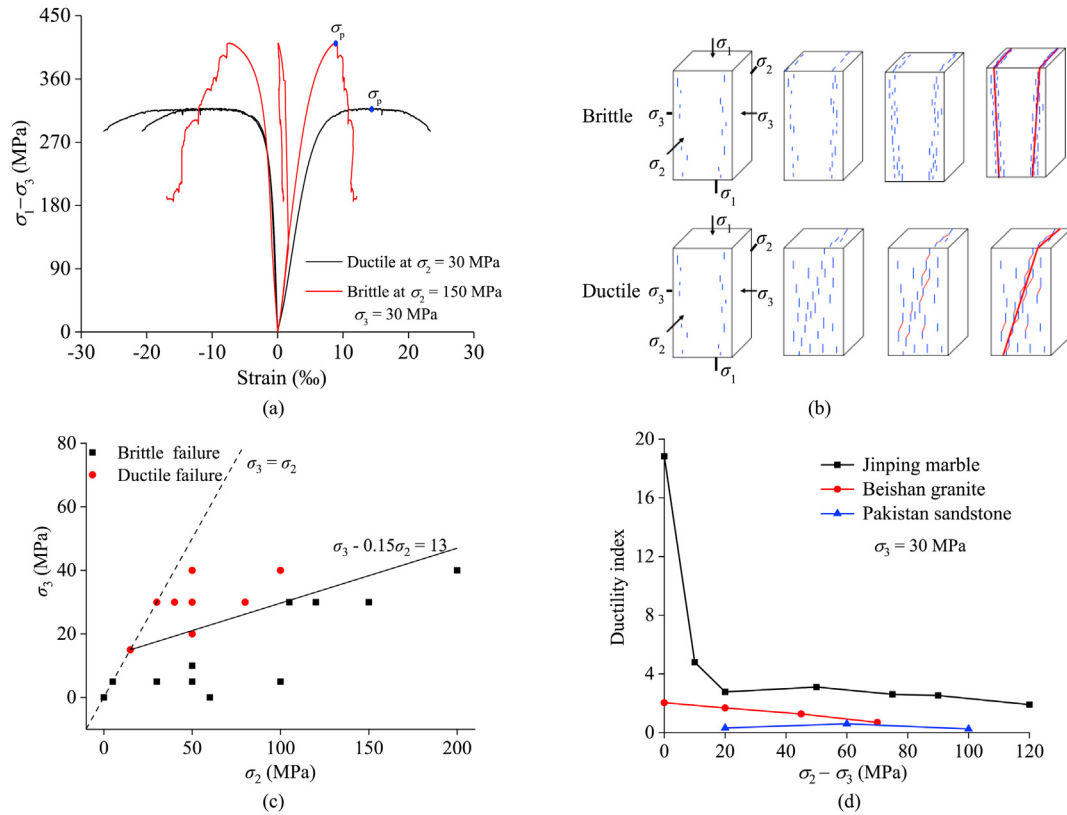


Fig. 30. Typical brittle and ductile characteristics of hard rocks: (a) Deformation characteristics, (b) Failure mechanism, (c) True triaxial stress boundary of the brittle-ductile transition of CJPL-II marble (Zhao et al., 2018), and (d) Changes in the ductility index of three rock types with increasing $\sigma_2 - \sigma_3$ at $\sigma_3 = 30$ MPa (Feng et al., 2021c).

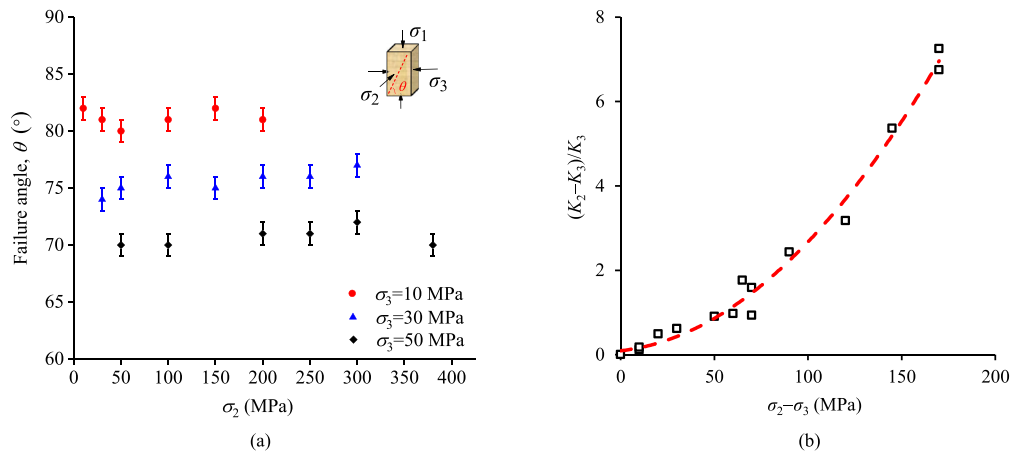


Fig. 31. (a) Variation in stress-induced failure angle for Yunnan sandstone of China and (b) deformation anisotropy degree of CJPL-II marble under true triaxial compression test. K_2 and K_3 represent the deformation moduli of the stress–strain curves in the σ_2 and σ_3 directions, respectively.

failure process, as shown in Fig. 4a. The strength of deep hard rocks is obviously stress-dependent and is affected by σ_2 and σ_3 (Kong et al., 2018). Increasing σ_3 can constantly increase the rock strength, but the strength of deep hard rocks exhibits asymmetric change characteristics with increasing σ_2 , i.e. first an increase and then a decrease (Fig. 32a). In the deviatoric plane, the failure envelope shows that the rock strength has an obvious Lode dependence (Fig. 32b). Similarly, σ_2 can increase the rock long-term strength but has little effect on the rock residual strength (Fig. 32c).

5.4. Effect of loading and unloading stress paths on the failure characteristics of deep hard rocks

True triaxial loading-unloading stress paths can make the failure of hard rock more severe and improve the failure strength. Table 2 compares the failure modes of CJPL-II marble under different true triaxial loading-unloading paths and true triaxial compression paths. The failure mode and severity of deep hard rocks are significantly influenced by the stress path. For example, CJPL-II marble shows a

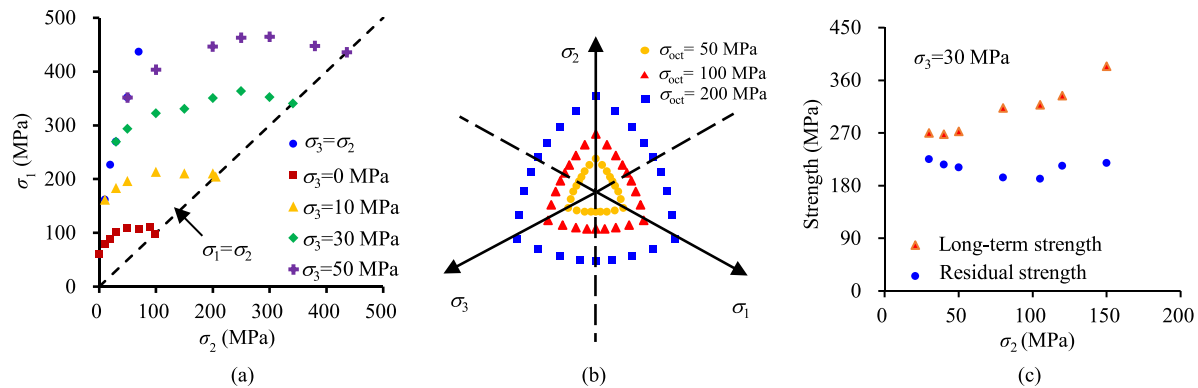


Fig. 32. True triaxial strength characteristics of hard rocks: (a) Asymmetric change characteristics of peak strength of Yunnan sandstone with the increase of σ_2 (Feng et al., 2019e), (b) Spherical triangle failure envelope with Lode dependence, and (c) Long-term and residual strength characteristics of CJPL-II marble.

Table 2

Failure modes of CJPL-II marble under true triaxial loading and unloading paths.

Item	True triaxial compression and unloading				True triaxial compression
	I	II	III	IV	V
Stress path					
Failure mode					

decreasing order of stress path: I > II > III > IV > V. The rock strength determined under the loading-unloading path is greater than that under the compression path, i.e. I > II > III > IV > V for CJPL-II marble (Fig. 33).

5.5. Effect of unloading rate on the failure characteristics of deep hard rocks

Under true triaxial stress, different unloading rates of σ_3 affect the failure strength and the unloading amount ($\Delta\sigma_3$) required for rock failure. Taking CJPL-II marble as an example, with increasing unloading rate, the unloading amount increases to ensure the failure of the rock samples (Fig. 34b). The difference in the bearing capacity between the loading and unloading tests decreases with decreasing unloading rate (Fig. 34c).

As shown in Fig. 35, with increasing unloading rate, the macroscopic failure mode of rock samples develops from tensile-shear failure to tensile fracture failure, with the failure becoming more severe. The transgranular failure caused by tension makes the microscopic fracture surface of the sample uneven, and numerous stepped tensile openings appear.

5.6. Effect of principal stress direction transformation on the failure characteristics of deep hard rocks

Principal stress direction transformation during true triaxial compression may play a controlling role in the development of brittle fracture, crack propagation and rock instability. As seen in

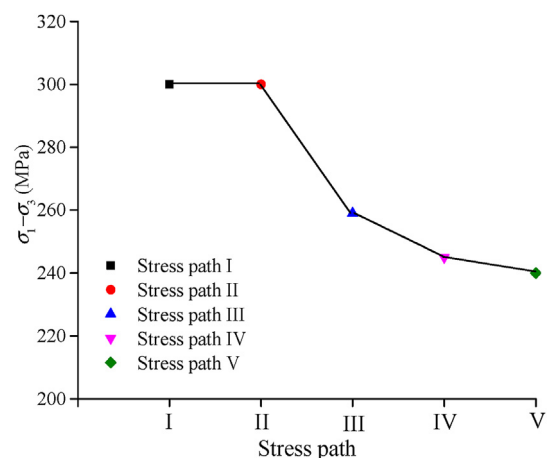


Fig. 33. Failure strength of CJPL-II marble with different stress paths under true triaxial compression (Xu et al., 2019).

Fig. 36, the transformation of the σ_1 and σ_2 directions at the post-peak stage can lead to a change in the crack propagation direction as the bearing capacity of the rock sample is improved. In the area where the direction of crack propagation changes, the walking direction of some grain river-like fracture patterns is deflected, and interlaced fracture characteristics appear in the grains (Fig. 36b). Since the propagation of brittle fracture under true triaxial compression depends on the σ_1 direction and the fracture is along

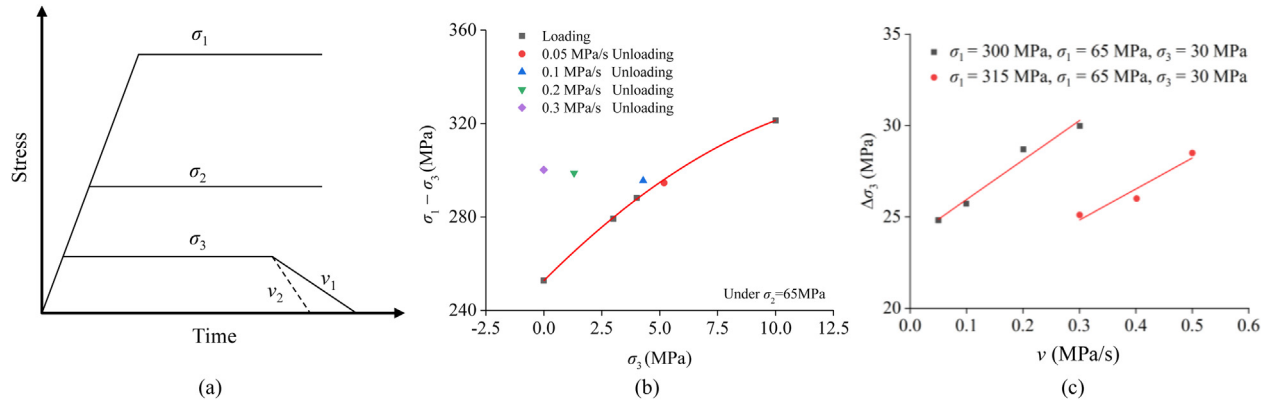


Fig. 34. Strength characteristics of CJPL-II marble with different unloading rates of σ_3 under true triaxial compression: (a) Stress path at different unloading rates of σ_3 , (b) Unloading amount of σ_3 ($\Delta\sigma_3$), and (c) Failure strength with increasing unloading rate of σ_3 .

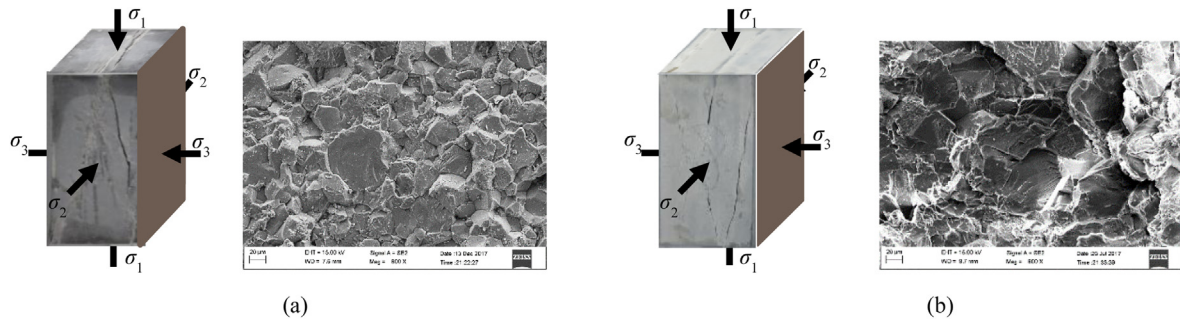


Fig. 35. Failure characteristics of CJPL-II marble with different unloading rates of σ_3 under true triaxial compression ($\sigma_1 = 300$ MPa, $\sigma_2 = 65$ MPa): (a) Unloading σ_3 rate of 0.01 MPa/s, and (b) Unloading σ_3 rate of 0.2 MPa/s (Xu et al., 2019).

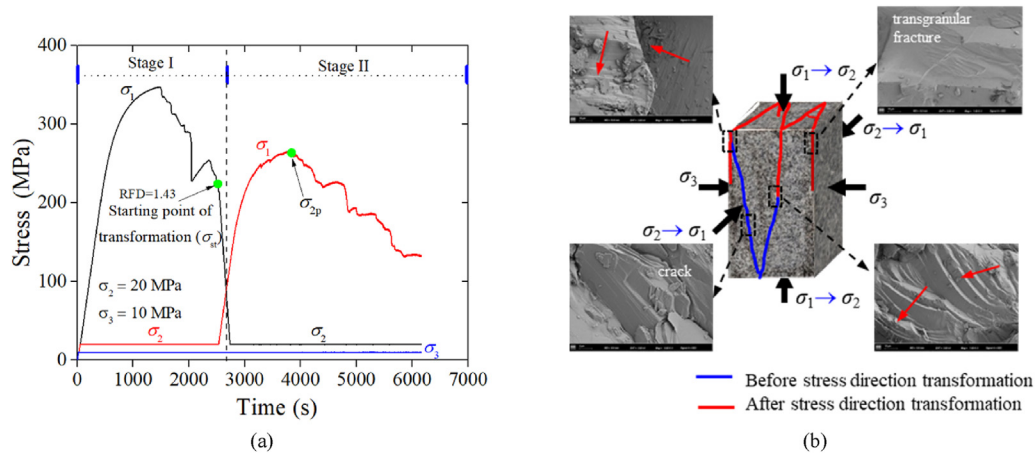


Fig. 36. Failure surface deflection and mechanism of Portugal granite induced by σ_1 and σ_2 direction transformation at the post-peak stage: (a) Stress vs. time diagrams of principal stress transformation, and (b) Failure surface and mechanism.

the σ_2 direction and inclined to the σ_3 direction, the anisotropic development of the stress direction transformation induces crack changes with the rotation of the new stress axis.

As shown in Fig. 37, with the increase in the principal stress transformation point of the rock sample recognized by the rock fracturing degree (RFD), the increment of the rock sample bearing capacity increases after the principal stress transforms. This is because after the transformation of the σ_1 and σ_2 directions, the crack development direction will not expand along the original crack development surface but will expand along the new crack growth direction. At that time, the fracturing degree in the new

crack development area is less than that of the original crack development area; thus, the strength will increase relatively; the greater the difference between the damage and rupture degree of the two areas, the greater the strength growth.

5.7. Effect of stiff joints on the failure characteristics of deep hard rock

Stiff joints can reduce the strength and increase the brittleness of deep hard rocks (Fig. 38) and affect the failure mode. Taking CJPL-II marble as an example, the failure types of jointed CJPL-II marble

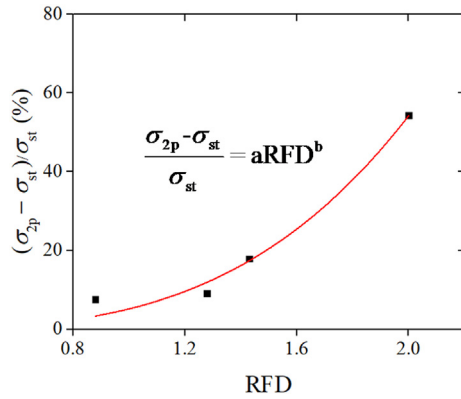


Fig. 37. Increasing percentage of rock sample bearing capacity of Portugal granite after principal stress direction transformation under different fracture degrees.

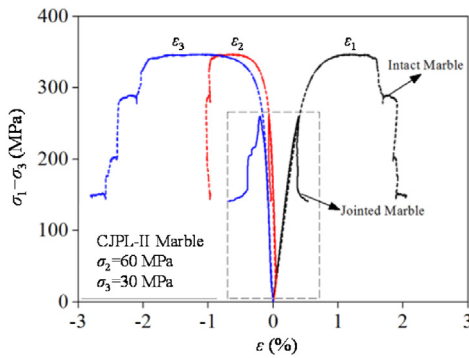


Fig. 38. Typical stress-strain curves of CJPL-II intact marble and jointed marble under true triaxial compression.

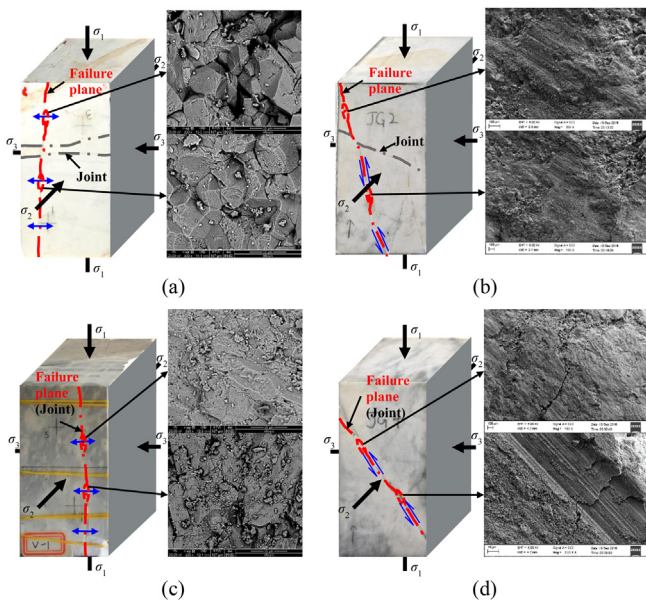


Fig. 39. Sketches of four distinct failure modes of the jointed CJPL-II marble under true triaxial compression: (a) Splitting of intact rock, (b) Shearing of intact rock, (c) Opening of the joint, and (d) Sliding along the joint (Gao et al., 2019).

samples can be divided into four categories depending on the spatial relationship between the joint occurrence and principal stress

directions, as seen in Fig. 39. σ_3 (perpendicular to the strike direction of the joint plane) roughly determines the tensile and shear failure mechanisms, while the inclination of the stiff joint greatly affects the tensile failure mechanism. Therefore, tensile failure and splitting failure easily occur under low σ_3 , and slip failure occurs only when the inclination of the stiff joint meets a specific angle. Shear failure and slip failure easily occur under high σ_3 .

5.8. Time-dependent failure and deformation mechanism of deep hard rocks

5.8.1. Creep characteristics of deep hard rocks

Due to the time effect, high stress causes aggregation of numerous tensile fractures in rocks, as shown in Fig. 6. Moreover, a high stress difference ($\sigma_2 - \sigma_3$) increases the brittleness and causes time-dependent failure with small deformation (Fig. 40a). The creep deformation of hard rock is caused by crack growth, and the creep deformation in the σ_3 direction is significantly higher than that in the σ_2 direction. This is because the creep failure process of hard rock caused by true triaxial stress is also directional. Due to the inhibitory effect of the high value of σ_2 , the number of cracks opening along the σ_2 direction is much lower than that opening along the σ_3 direction (Fig. 40b). The differential creep deformation of CJPL-II marble in the σ_2 and σ_3 directions is unaffected by σ_1 and time and is merely influenced by σ_2 and σ_3 , as shown in Fig. 40c (Zhao et al., 2021b).

5.8.2. Relaxation characteristics of deep hard rocks

As seen in Fig. 41, the antistress relaxation ability at the post-peak stage is significantly lower than that at the pre-peak stage (Fig. 41a). The time-dependent deformation of ϵ_2 gradually transforms from dilation to compression when σ_2 is very high (Fig. 41b). This is because the cracks in the ϵ_2 direction are inhibited by the high value of σ_2 . Moreover, a reduction in axial stress leads to rebound of the compression deformation in the ϵ_2 direction. The dilation caused by crack propagation in the ϵ_3 direction is greater than the compression deformation triggered by the reduction in axial stress under a high axial stress (Fig. 41c).

5.9. Stress-induced failure difference in deep hard surrounding rock

During deep hard rock excavation, the surrounding rocks from the excavation surface to the interior may experience different stress paths and therefore show different mechanical characteristics and failure mechanisms. As shown in Fig. 42, taking the laboratory and field test results in tunnel No. 7 of CJPL-II as an example, it can be seen that the failure of the surrounding rocks is asymmetrical. Near the sidewall, low (unloading) σ_3 leads to super-brittle behavior of the rock with mainly tensile failure, approximately parallel to the σ_1 direction, which is almost parallel to the excavation surface. With increasing depth into the surrounding rocks, as σ_3 increases, the stress-induced brittleness decreases, while the ductility increases gradually; thus, the proportion of shear cracking during failure increases.

6. Mechanical analysis method for deep hard rock excavations

6.1. 3D nonlinear failure criterion for deep hard rocks

Considering the stress-induced failure characteristics of deep hard rocks, a 3D hard rock failure criterion (3DHRFC) was proposed by Feng et al. (2019e), which is written as follows:

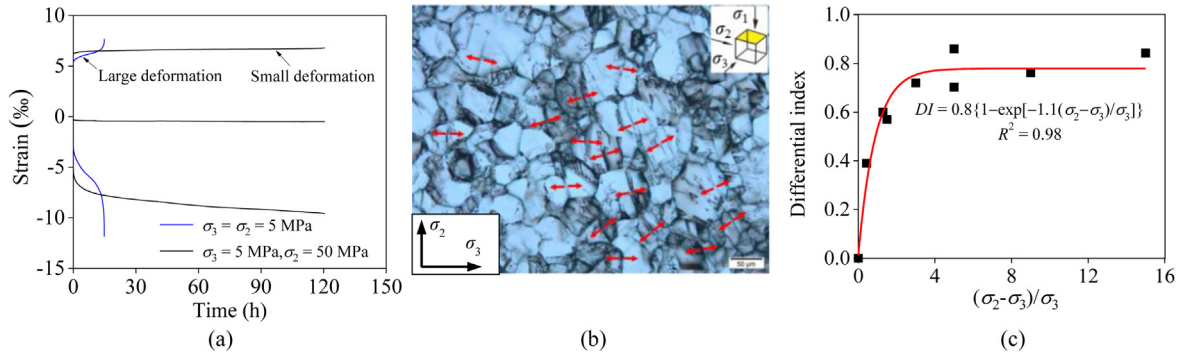


Fig. 40. Creep characteristics of hard rocks under true triaxial compression: (a) Strain-time curve of Beishan granite under conventional and true triaxial conditions; (b) Most of the microcracks open along the σ_3 direction in the σ_2 – σ_3 plane in CJPL-II marble; and (c) Effects of σ_2 and σ_3 on the differential creep deformation of CJPL-II marble in the σ_2 and σ_3 directions (Zhao et al., 2021b). DI is the ratio of the difference in the creep deformation increment in the σ_3 and σ_2 directions to the creep deformation increment in the σ_3 direction.

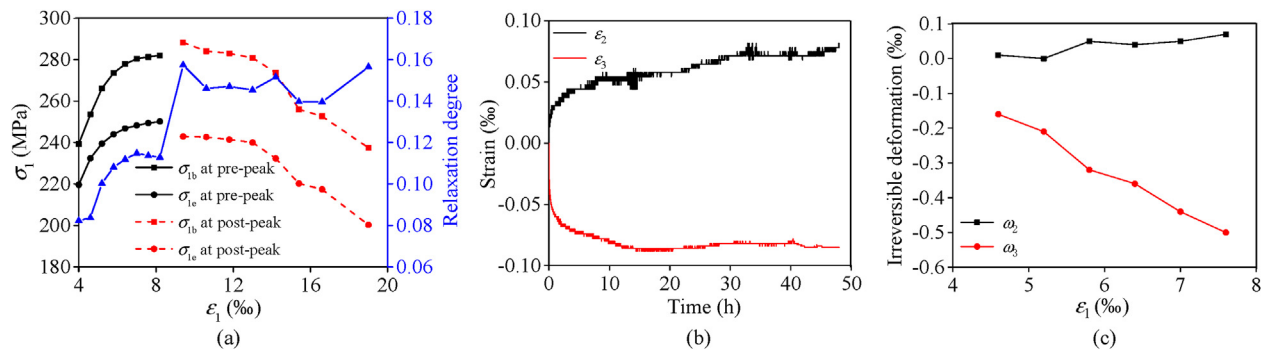


Fig. 41. Relaxation characteristics of CJPL-II marble under true triaxial compression: (a) Stress relaxation degree $((\sigma_{1b} - \sigma_{1e})/\sigma_{1b})$ at each relaxation stage at $\sigma_3 = 20$ MPa and $\sigma_2 = 50$ MPa, where σ_{1b} and σ_{1e} are the starting and end points of stress relaxation, respectively; (b) Strain-time curves; and (c) Irreversible deformations induced by long-term relaxation testing at $\epsilon_1 = 4.6\%$, $\sigma_3 = 20$ MPa, and $\sigma_2 = 120$ MPa (Zhao et al., 2021c). w_2 and w_3 are the irreversible viscoplastic deformation induced by axial stress relaxation in the σ_2 and σ_3 directions, respectively.

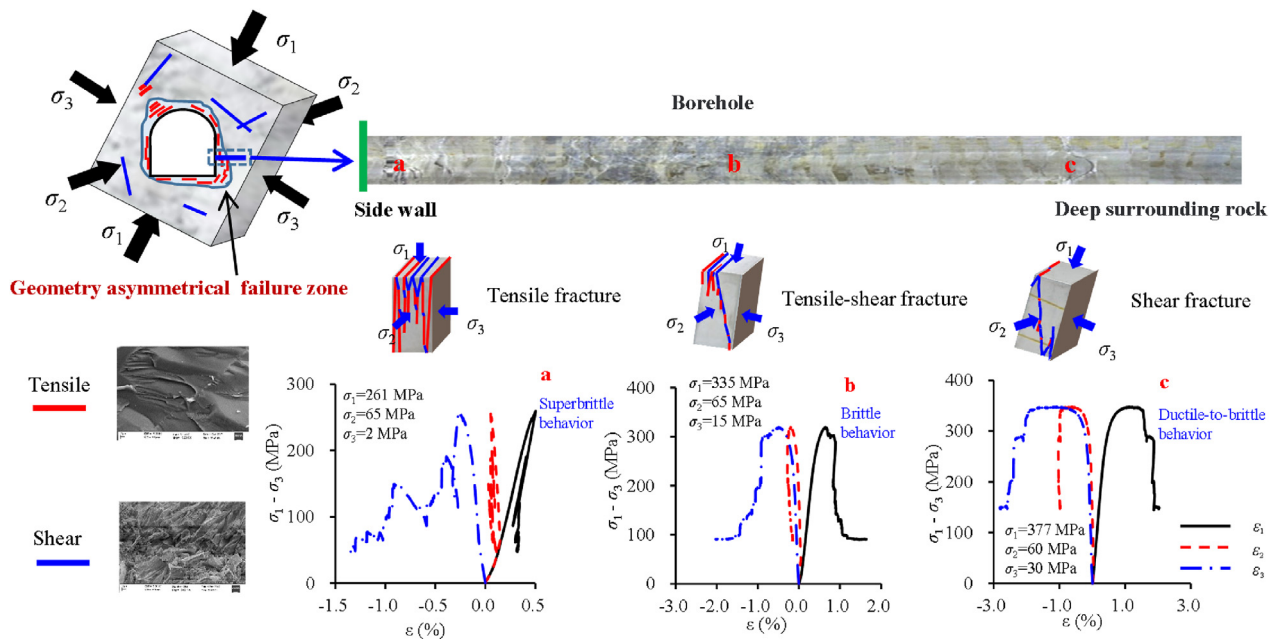


Fig. 42. Stress-induced failure mechanism of the hard surrounding rocks of tunnel No. 7 of CJPL-II from the sidewall to the interior. a, b and c indicate the rock sampling positions.

$$\left(\frac{\sigma_1 - \sigma_3}{\sin \varphi}\right)^2 = \frac{(\sigma_1 + \sigma_3 + 2c \cot \varphi)^2 - (2\sigma_t + 2c \cot \varphi)^2}{\left[\sqrt{1 - b + sb^2} + t(1 - \sqrt{1 - b + b^2})\sin \varphi\right]^2} \quad (2)$$

where c , φ and σ_t are the cohesion, internal friction angle and tensile strength of rock, respectively; b is the intermediate principal stress coefficient, and $b = (\sigma_2 - \sigma_3)/(\sigma_1 - \sigma_3)$; and s and t are the material parameters. s reflects the strength difference under $\sigma_2 = \sigma_3$ and $\sigma_1 = \sigma_2$, and t controls the increased percentage in the rock strength caused by σ_2 .

The 3DHRFC has the following characteristics:

- (1) The failure strength envelope asymmetrically changes with increasing σ_2 ; this is highly consistent with the experimental results (Fig. 43a). The asymmetry reflects the strength difference under generalized triaxial compression stress

($\sigma_1 > \sigma_2 = \sigma_3$) and generalized triaxial extension stress ($\sigma_1 = \sigma_2 > \sigma_3$).

- (2) The 3D failure envelope can have different shapes in the deviatoric plane, such as spherical triangles, triangles, circles and hexagons. As a result, the stress Lode dependence of the failure strength can be well reflected (Fig. 43b).
- (3) The envelope also has nonlinear characteristics in the meridian plane, and the stress region is divided based on different failure mechanisms, as shown in Fig. 43c.

6.2. Stress-induced brittle-ductile anisotropic model for deep hard rocks

To reflect the brittle and ductile failure, deformation characteristics, stress-induced fracturing, and deformation anisotropy of deep hard rocks, a 3D anisotropic brittle-ductile failure mechanical model for hard rocks is established (Feng et al., 2021d). The model can be written as follows:

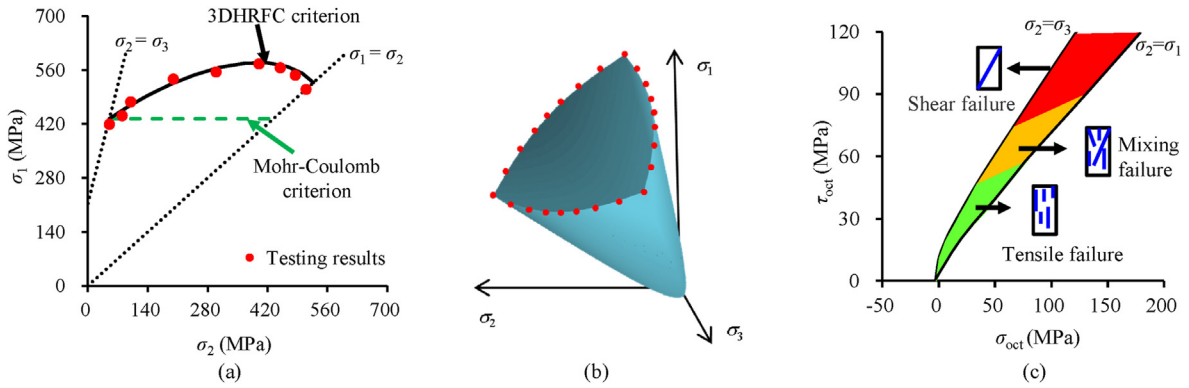


Fig. 43. Characteristics of the 3DHRFC criterion: (a) Asymmetric change in rock strength with increasing σ_2 , (b) 3D failure envelope with Lode dependence, and (c) Zoning characteristics of the failure mechanism (Feng et al., 2019e).

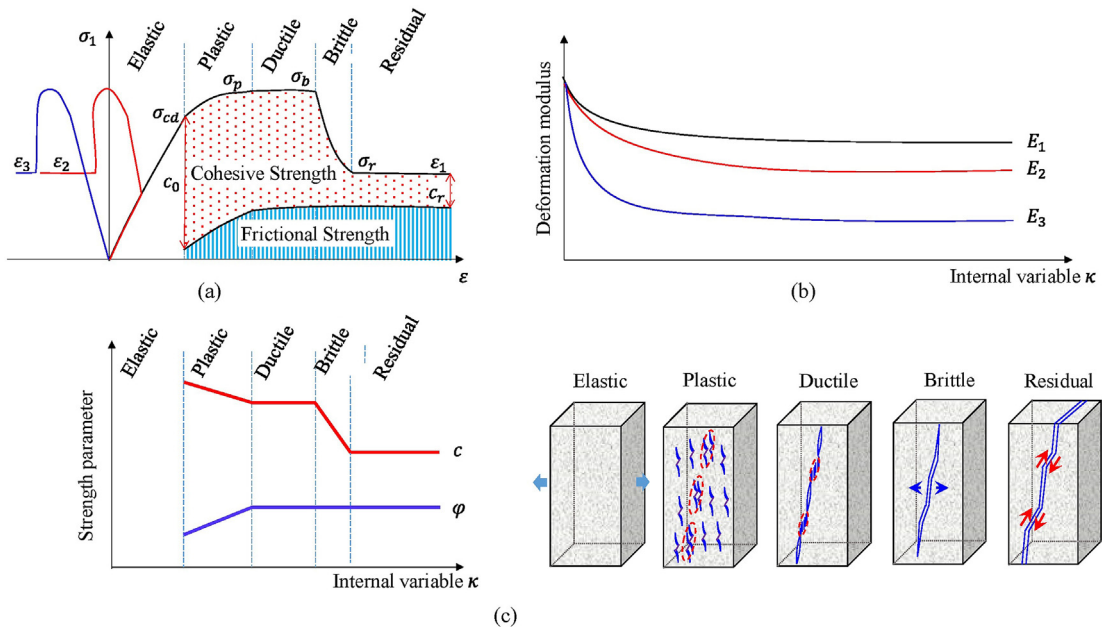


Fig. 44. Main characteristics of the 3D stress-induced brittle-ductile anisotropic failure model: (a) 3D stress-dependent brittleness and ductility, (b) Stress-induced deformation anisotropy based on modulus evolution, and (c) Rock fracturing process based on strength parameter evolution (Feng et al., 2021d).

$$\dot{\sigma} = \mathbf{E}^a(\kappa) \cdot (\dot{\epsilon} - \dot{\epsilon}^p) \quad (3)$$

$$\kappa = \overline{\epsilon}^p \cdot Brit(\sigma_2, \sigma_3) \quad (4)$$

$$Brit(\sigma_2, \sigma_3) = \frac{1}{(\sigma_3/UCS + D)e^{-\sigma_2/UCS}} \quad (5)$$

$$\dot{\epsilon}^p = A \frac{\partial Q}{\partial \sigma} \quad (6)$$

$$c = c_0 - \sum w_i \Delta \kappa_i (c_0 - c_r) \quad (7)$$

$$\varphi = \varphi_0 + \sum s_i \Delta \kappa_i (\varphi_r - \varphi_0) \quad (8)$$

$$E_j = E_0 d_j(\sigma_2, \sigma_3, \kappa, R_2, R_3) \quad (9)$$

stiffness tensor based on the deformation modulus E_j in the three principal stress directions calculated in Eq. (9). More details can be found in Feng et al. (2021d).

The model has the following characteristics:

- (1) The stress-induced brittleness and ductility of deep hard rocks are quantitatively defined to model the stress-strain behavior, especially at the post-peak stage (Fig. 44a).
- (2) The stress-induced deformation anisotropy is described via the deformation modulus evolution in the three principal directions (Fig. 44b).
- (3) The elastic, plastic, brittle and ductile deformations are reflected by the evolution of the strength parameters, where different variations in cohesion and internal friction angle can realize different fracturing mechanisms (Fig. 44c).
- (4) The model can be degenerated into some classical failure mechanical models.

$$\begin{bmatrix} \dot{\epsilon}_1^{vp} & \dot{\epsilon}_{12}^{vp} & \dot{\epsilon}_{13}^{vp} \\ \dot{\epsilon}_{21}^{vp} & \dot{\epsilon}_2^{vp} & \dot{\epsilon}_{23}^{vp} \\ \dot{\epsilon}_{31}^{vp} & \dot{\epsilon}_{32}^{vp} & \dot{\epsilon}_3^{vp} \end{bmatrix} = \gamma_1 \begin{bmatrix} 1 & \frac{1+A+AB}{2} & \frac{1+A}{2} \\ \frac{1+A+AB}{2} & A(1-B) & \frac{A(2-B)}{2} \\ \frac{1+A}{2} & \frac{A(2-B)}{2} & A \end{bmatrix} \langle \Phi \rangle \frac{\partial F_1}{\partial \sigma_{ij}} \quad (10)$$

where $\dot{\sigma}$, $\dot{\epsilon}$ and $\dot{\epsilon}^p$ are the incremental stress and strain tensors and the incremental plastic strain tensor, respectively; c_0 , φ_0 and E_0 are the initial values of cohesion, internal friction angle and Young's modulus, respectively; κ is the internal variable; κ_i represents the threshold of κ ; $\overline{\epsilon}^p$ is the equivalent plastic strain; $Brit$ is a brittleness index; D is a brittle parameter; A is the plastic multiplier; Q is the plastic potential; w_i and s_i are the decreasing rate of cohesion c and increasing rate of internal friction angle φ , respectively; d_j is the deterioration function of the deformation modulus in the three principal stress directions; R_2 and R_3 are the model anisotropic parameters; and $\mathbf{E}^a(\kappa)$ is the stress-induced anisotropic elastic

6.3. Stress-induced anisotropic time-dependent failure model for deep hard rocks

The time-dependent failure and deformation behaviors of deep hard rocks are affected by true triaxial stress-induced brittle and ductile characteristics (Fig. 45). During brittle creep, the relationship between the creep rate and 3D stress state evolves linearly, while it evolves nonlinearly during ductile creep.

To reflect the influences of the brittle-ductile transition, true triaxial stress and the tensile fracture mechanism in the rheological process of deep hard rocks, the time-dependent deformation difference caused by the brittle-ductile transition, the anisotropy of the time-dependent failure in three principal stress directions caused by true triaxial stress, and the strength parameter weakening caused by tensile fracture are considered in the model. The model can be written as follows:

$$A = l_1 \exp\left(\frac{l_2 \sigma_3}{\sigma_1 - \sigma_3}\right) + l_3 \quad (11)$$

$$B = n_1 \left\{ 1 - \exp\left[\frac{n_2(\sigma_2 - \sigma_3)}{\sigma_{UCS}}\right] \right\} \quad (12)$$

$$\langle \Phi \rangle = \begin{cases} 0 & (F \leq 0) \\ k_1 \left(\frac{\lambda \sigma_{UCS}}{\sigma_{OCT}}\right) + k_2 & (F > 0, \sigma_3 - 0.15\sigma_2 \leq 13) \\ k_3 \left(\frac{\lambda \sigma_{UCS}}{\sigma_{OCT}}\right)^{k_4} & (F > 0, \sigma_3 - 0.15\sigma_2 > 13) \end{cases} \quad (13)$$

$$c = (1 - D)c_0 + c_1 \quad (14)$$

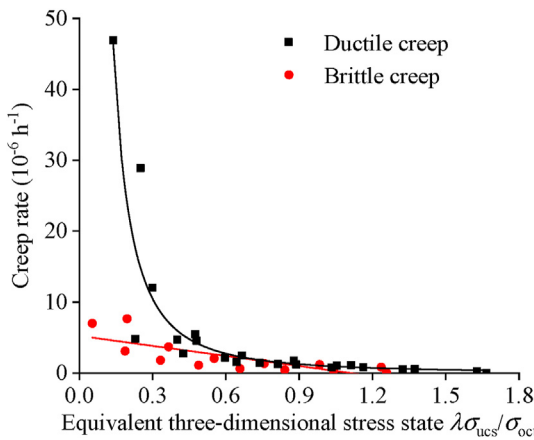


Fig. 45. Relationship between the axial steady creep rate and $\lambda \sigma_{UCS}/\sigma_{OCT}$ of CJPL-II marble under the true triaxial creep test. Parameter λ is used to express the 3D stress state; σ_{UCS} and σ_{OCT} are the uniaxial compressive strength and octahedral normal stress, respectively.

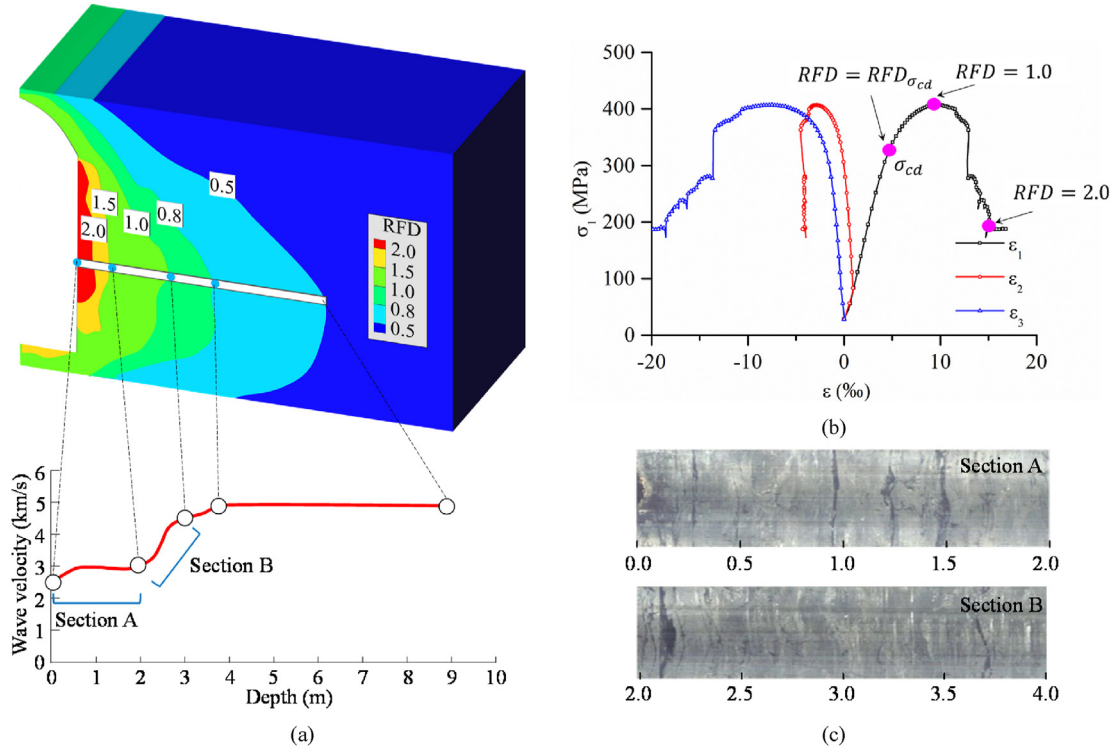


Fig. 46. (a) Simulated RFD result during the excavation of tunnel No. 7 of CJPL-II; (b) Thresholds of the RFD values corresponding to different stages in the typical stress-strain curve of CJPL-II marble under true triaxial compression (Feng et al., 2021e); and (c) The fracture characteristics of Sections A and B measured by a borehole camera, with five main fractures in Section A corresponding to $RFD = 1.5$ – 2 and two main fractures in Section B corresponding to $RFD = 1$ – 1.5 .

where ε_{ij}^{vp} is the viscoplastic strain; γ_1 is the viscoplastic flow coefficient in the σ_1 direction; D is the damage variable; c_0 and c_1 are the initial and residual cohesions, respectively; l_1, l_2, l_3, n_1 and n_2 are the viscoplastic flow anisotropy parameters; and k_1, k_2, k_3 and k_4 are the deformation parameters. These parameters can be determined through the true triaxial creep test.

6.4. RFD index

To assess the fracturing degree of deep hard rocks, a new index called RFD is defined as

$$RFD = \begin{cases} 1 - \frac{g(\theta)\sqrt{Ap^2 + Bp + C} - q}{g(\theta)\sqrt{Ap^2 + Bp + C}} & (F < 0) \\ 1 + \max\left(\frac{\varepsilon_s^p}{\varepsilon_s^{p-lim}}, \frac{\varepsilon_t^p}{\varepsilon_t^{p-lim}}\right) & (F \geq 0) \end{cases} \quad (15)$$

$$RFD = \begin{cases} RFD_{\sigma_{cd}} \text{ to } 1 & (\text{Pre-peak fracture}) \\ 1 - 2 & (\text{Post-peak fracture}) \\ 2 & (\text{Complete structural failure}) \end{cases} \quad (16)$$

where $[g(\theta)\sqrt{Ap^2 + Bp + C} - q]/[g(\theta)\sqrt{Ap^2 + Bp + C}]$ is the yield proximity and $\max(\varepsilon_s^p/\varepsilon_s^{p-lim}, \varepsilon_t^p/\varepsilon_t^{p-lim})$ is the measurement of inelastic failure at the post-peak stage, which considers both the influences of the plastic volume change and plastic distortion; $RFD_{\sigma_{cd}}$ is the RFD value at the crack damage stress σ_{cd} ; $g(\theta)$ is the shape function of the Lode angle θ in the deviatoric plane; p is the mean principal stress; q is the equivalent shear stress; and ε_s^p and ε_t^p are the

plastic volumetric strain and equivalent plastic shear strain, respectively. Correspondingly, ε_s^{p-lim} and ε_t^{p-lim} are their limit values that can be determined from biaxial and conventional triaxial compression tests (Feng et al., 2021d). The RFD is constrained to be less than or equal to 2. If the value exceeds 2, set it to 2.

The RFD index can be used to assess the location, depth and degree of rock fracturing. As illustrated in Fig. 46, the simulated RFD result matches well with the fracturing location and depth observed through wave velocity variation. A comparison between the simulated results and fracturing degree revealed by the borehole camera results (Fig. 46c) indicates that the RFD index is able to reflect the fracturing degree in the field.

6.5. LERR index

To quantitatively analyze the strength of the brittle fracture of an engineering rock mass, based on the understanding of its failure phenomenon characterized by energy release, a new index called the local energy release rate (LERR) is proposed, i.e. the energy is suddenly released per unit volume (volumetric rate) of engineering rock mass when the locally accumulated strain energy exceeds the limit storage energy during the fracturing process of an engineered rock mass (Su et al., 2006). This index is an approximate expression of the released energy per unit brittle failed rock mass and can be used as a quantitative index to reflect the brittle failure intensity. The specific expression of LERR is

$$LERR = U_{\max} - U_{\min} \quad (17)$$

$$U_{\max} = \frac{\sigma_1^2 + \sigma_2^2 + \sigma_3^2 - 2\nu(\sigma_1\sigma_2 + \sigma_2\sigma_3 + \sigma_3\sigma_1)}{2E} \quad (18)$$

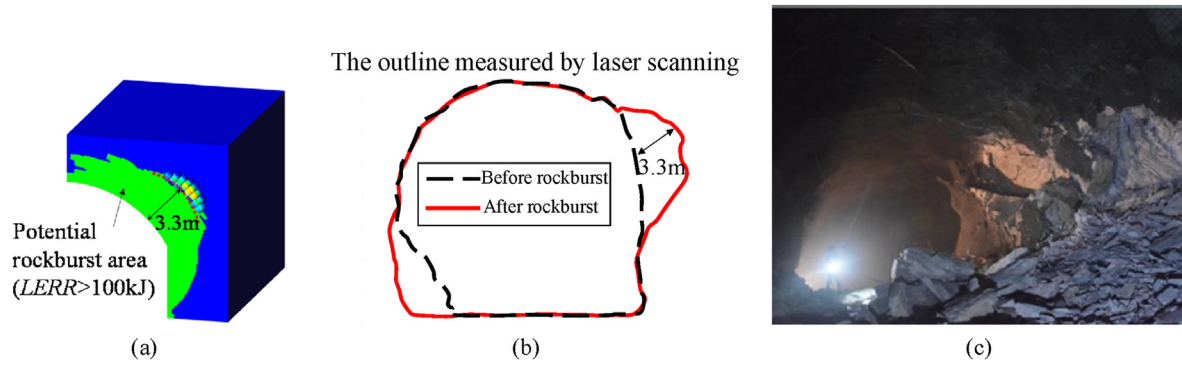


Fig. 47. Assessing the rockburst depth and energy release by LERR (an intensive rockburst case during the excavation of tunnel No. 8 of CJPL-II, for example): (a) The potential rockburst area calculated by $LERR > 100$ kJ, (b) The outline change before and after rockburst measured by laser scanning, and (c) Site photo of the rockburst.

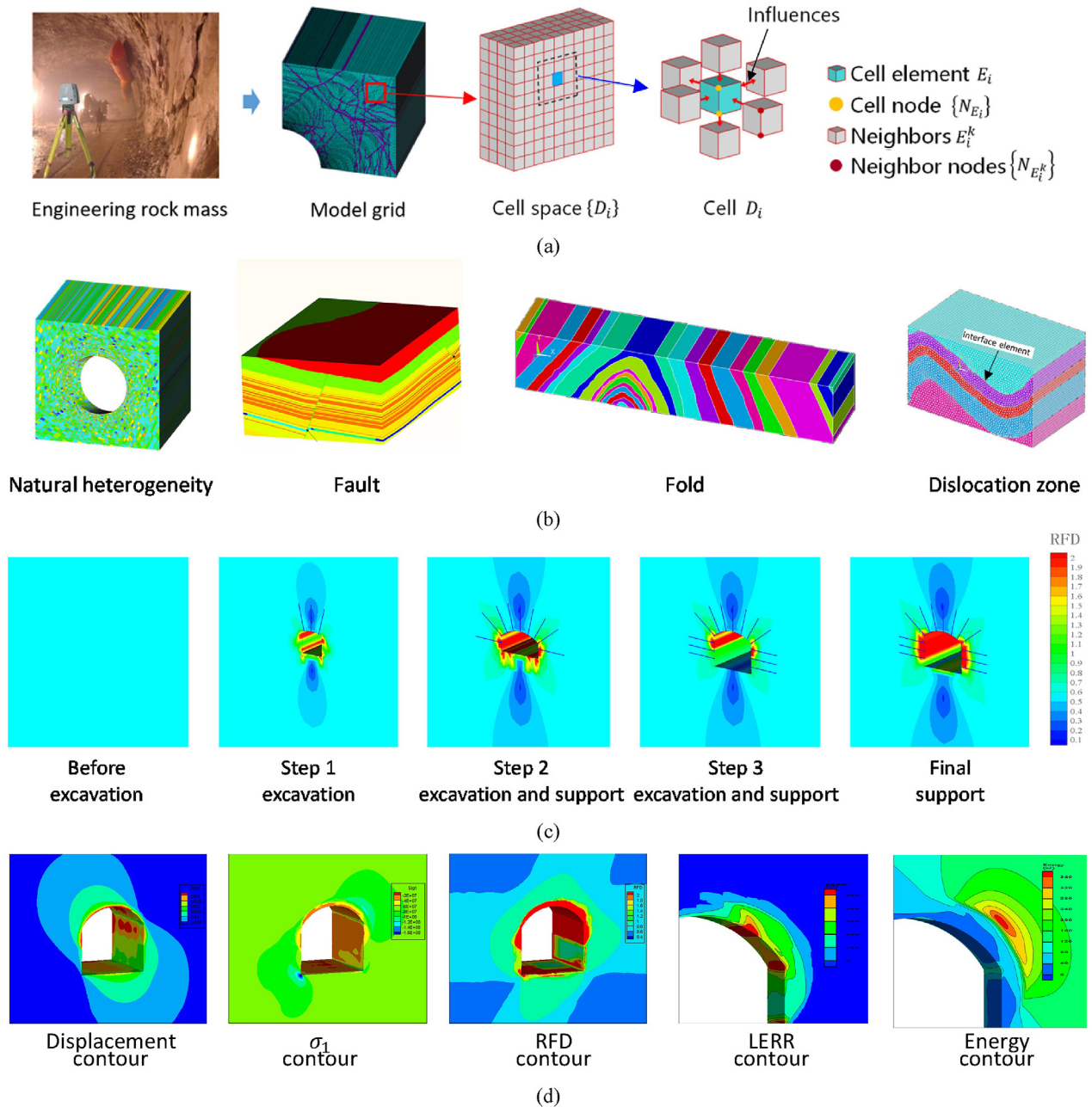


Fig. 48. Main characteristics of CASRock: (a) Local analysis method based on cellular automata: a rock mass discretized into cells and local updating, with cells, neighbors and their influences also being illustrated (Feng et al., 2021e); (b) Natural heterogeneity, fault, fold and dislocation zone representation through the digital reconstruction method; (c) Multistep excavation and support of a D-shaped tunnel by the excavation and support design module; and (d) CASRock simulation results of a deep hard rock tunnel excavation, and the results indicate high energy release, severe failure, small deformation and high energy and stress concentrations.

$$U_{\min} = \frac{\sigma_1'^2 + \sigma_2'^2 + \sigma_3'^2 - 2\nu(\sigma_1'\sigma_2' + \sigma_2'\sigma_3' + \sigma_3'\sigma_1')}{2E} \quad (19)$$

where E and ν are the deformation modulus and Poisson's ratio of the rock mass, respectively; U_{\max} and U_{\min} are the maximum and minimum values of the elastic strain energy density before and after brittle failure, respectively, which are both dependent on 3D stresses; and σ_1' , σ_2' and σ_3' are the maximum, intermediate and minimum principal stresses of the rock mass after brittle failure, respectively.

The LERR can be used to directly reflect the complex situation in which the limited storage energies of different points of different positions of a rock mass are different under the engineering excavation stress state and can consider the energy release, energy transfer and plastic property dissipation of the surrounding rocks in a series of complex energy dynamic processes (Fig. 47).

6.6. Numerical analysis method and software

To predict the excavation-induced deep hard rock fracturing process and evolution process of stress-induced disasters, a 3D numerical analysis method, cellular automata software for the engineering rock mass fracturing process (CASRock), has been developed (Feng et al., 2006, 2021e). It has the following characteristics:

- (1) As a local analysis method based on cellular automata, it provides simulation of cracking (localization process) in deep hard rocks, which presents violent fracturing with small deformation, considering rocks as an assembly of heterogeneous deformable cells that interact with each other, and focusing on local cell fractures and the corresponding influence on the neighbors, as well as the self-organization propagation of cellular automata (Fig. 48a). This is consistent with the natural cracking process of deep rock masses.
- (2) The structural characteristics of deep rock masses, such as natural heterogeneities, internal defects, joints and discontinuities, as well as complex geological structures, such as faults, hard structural planes, columnar joints, folds, dislocation zones and dikes, are considered by means of digital sampling or digital reconstruction methods (Fig. 48b).
- (3) The method includes the above-mentioned 3D nonlinear failure criterion, brittle-ductile anisotropic failure model, stress-induced anisotropic time-dependent failure model, RFD, LERR, and other conventional models.
- (4) The method reproduces the excavation process, including drill-and-blast excavation, TBM excavation,

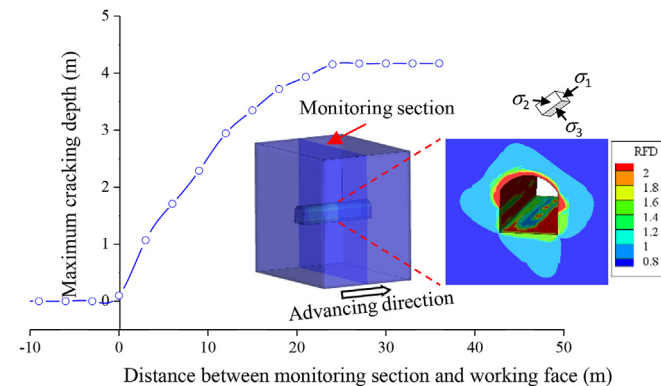


Fig. 49. Evolution curve of the maximum cracking depth of the surrounding rocks with respect to the excavation process in the CJPL-II deep tunnel.

stress release and field reinforcement. It also includes modules of back analysis of rock mechanical parameters and of 3D in situ stress field, excavation and support design (Fig. 48c), disaster prediction and engineering stability analysis.

CASRock has been applied to various areas in deep hard rock excavations, including water conservancy and hydropower engineering, high-level nuclear waste disposal, CO₂ geological sequestration, coal mining engineering, etc. More applications of CASRock can be found in Figs. 46, 47 and 48d.

7. Control principles and methods of stress-induced disasters in deep hard rock excavations

7.1. Cracking-restraint method for excavation and support optimization design

Since spalling, deep cracking, large deformation and collapse in deep hard rock excavations are mainly attributed to the evolution and transfer of internal cracking, the cracking-restraint method is developed to optimize the excavation scheme, support parameters and support time to minimize the range, depth and degree of internal cracking in surrounding rocks (Feng et al., 2016; Jiang et al., 2019). The cracking-restraint method is described as

$$\text{optimize}\{S\}:\text{minimize}\{D_{\max}|RFD \in [0.85, 1]\} \subseteq \{D_{\text{acceptable}}\} \quad (20)$$

$$\begin{aligned} \text{optimize}\{L, P, T\}:\text{minimize}\{D_{\max}|RFD \in [0.85, 1], RFD_{\max}\} \\ \subseteq \{D_{\text{acceptable}}, 2\} \end{aligned} \quad (21)$$

where S is the excavation scheme, including the excavation sequence, bench height, and rate; L , P and T are the length, intensity and time of support, respectively; D_{\max} is the cracking depth represented by the RFD index; and $D_{\text{acceptable}}$ is some acceptable fracturing depth for a particular deep engineering. The $D_{\text{acceptable}}$ can be determined either by experience or by theoretical analysis. If sufficient experience was gained from previous similar engineering projects, $D_{\text{acceptable}}$ can be chosen as the maximum fracturing depth under which the engineering stability can still be maintained. The $D_{\text{acceptable}}$ can also be estimated by some indices reflecting the fracturing property of deep hard rocks, such as the RFD index

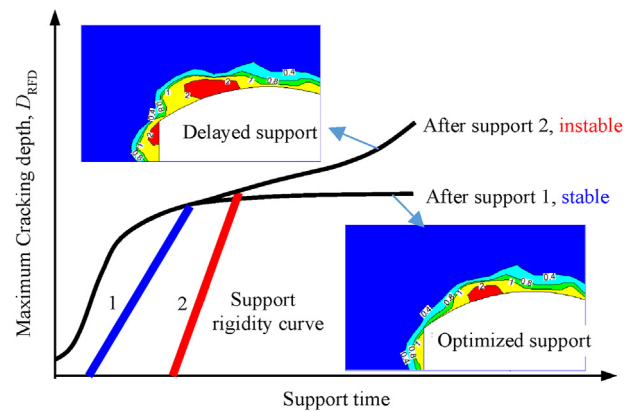


Fig. 50. Schematic of the principle of the cracking-restraint method. Case 1 represents a reasonable support time with the subsequent growth of cracking being controlled effectively, while Case 2 represents support that occurs too late, leading to excessive cracking.

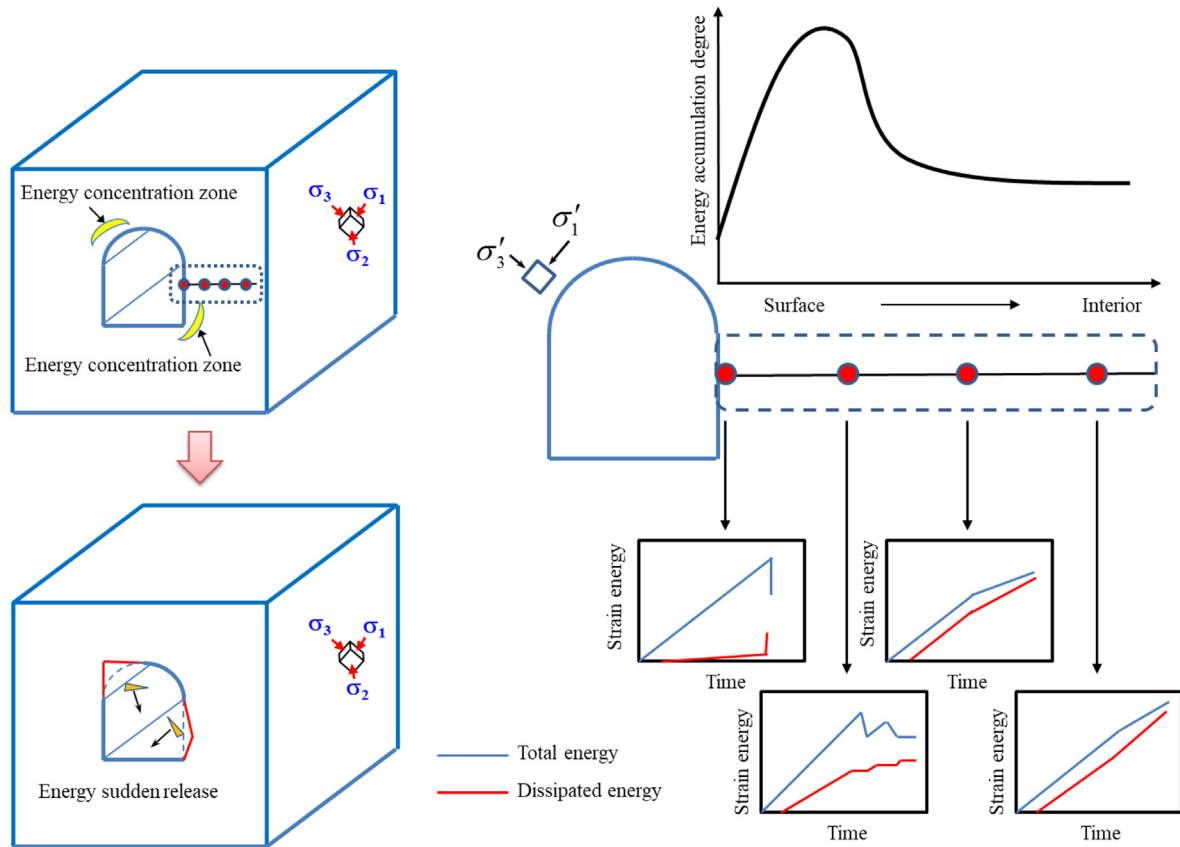


Fig. 51. Energy storage and release capacity of the rock mass from the surface to the interior in the deep surrounding rock mass.

proposed in this paper. Different RFD values can be linked to different fracturing degrees of deep hard rocks. The $D_{\text{acceptable}}$ can be chosen as the maximum depth encircled by the maximum RFD value in a tentative numerical simulation considering the most unfavorable conditions.

The typical cracking evolution feature of deep hard rocks with respect to the excavation process is illustrated by numerical simulation of a deep tunnel in the CJPL-II project. The maximum

cracking depth around the tunnel is determined by finding the maximum distance between the D_{max} contour and the excavation boundary, and this value is plotted against the distance between the monitoring section and working face (Fig. 49). In this figure, we can see that when the working face approaches the monitoring section, the cracking depth continues to increase with the excavation process until the working face is far away from the monitoring section. If the support measures are not installed in time, the

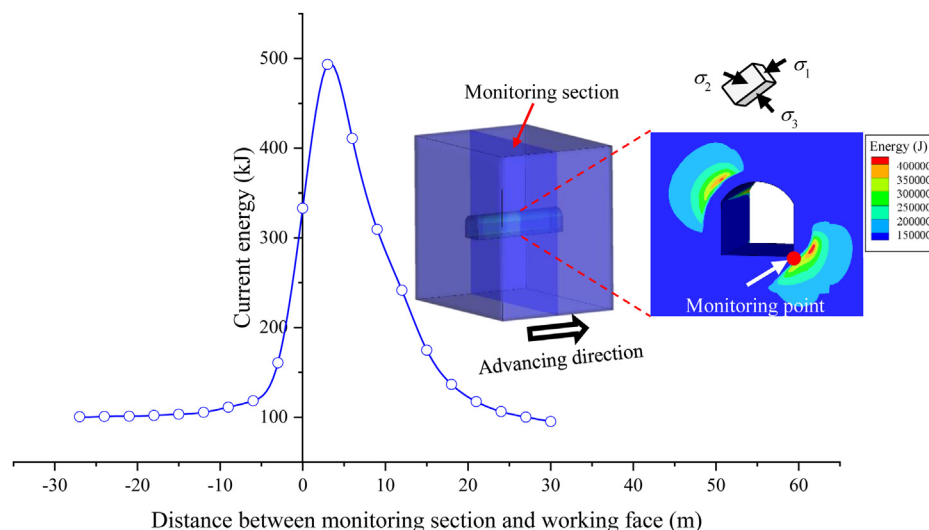


Fig. 52. Energy evolution curve of surrounding rocks with respect to the excavation process in the CJPL-II deep tunnel.

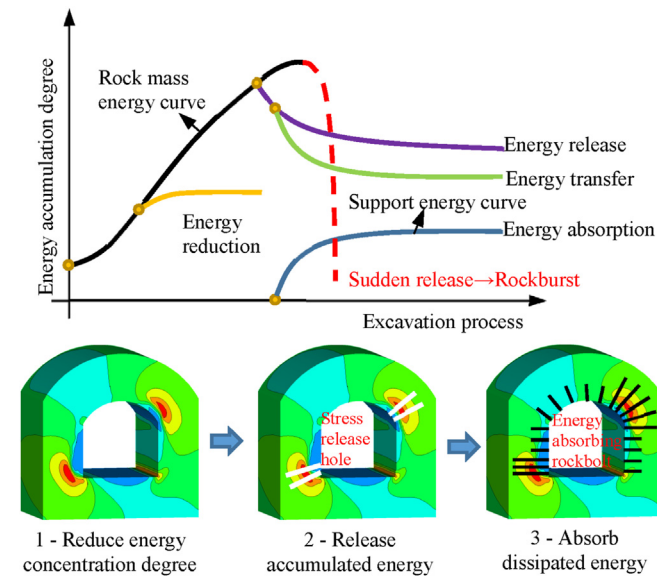


Fig. 53. Basic principles and techniques of the energy-controlled method for excavation and support optimization design.

maximum cracking depth can grow to an unacceptable level, leading to disastrous results. Field monitoring results also support this kind of cracking evolution characteristic in deep hard rock engineering (Feng et al., 2016b).

Based on the conceptual understanding of the cracking evolution characteristics of deep hard rocks and the principle that catastrophic cracking development must be prevented, a reasonable excavation scheme or support parameter/time should be determined. Fig. 50 shows the variation in the maximum cracking depth with respect to support time (represented by the distance between the monitoring position and working face). As shown in Case 1, if a reasonable support time can be realized, the subsequent growth of cracking can be controlled effectively. In Case 2, the support is too late, leading to an excessive cracking depth.

7.2. Energy-controlled method for excavation and support optimization design

Rockbursts in deep engineering usually exhibit a sudden release of stored strain energy, leading to catastrophic consequences such as rockburst. From the energy release capacity of deep rocks shown in Fig. 51, it can be deduced that the energy storage capacity of the

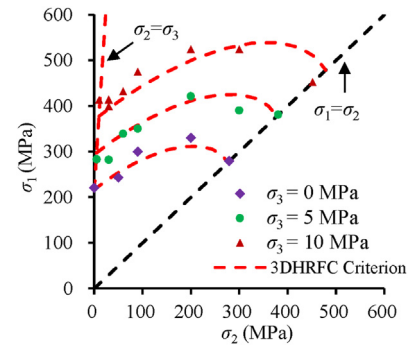


Fig. 55. True triaxial strength of the basalt under different stresses.

rock mass is strengthened from the surface to the interior, suggesting that the interior rock mass may accumulate a large amount of energy. This provides an energy source for intense rockburst. The energy release capacity, however, decreases from the surface to the interior, which means that the failure mode of the rock mass varies with depth. On the surface, once the stored energy is released, brittle cracking can easily occur. At the positions slightly deeper, there is a zone in which the stored energy may be released several times. At deeper places in the rock mass, there is a zone in which the strain energy may experience a storage-gentle release-sudden release process. In this zone, intense or extremely intense rockburst may occur.

The typical energy evolution feature of deep hard rocks with respect to the excavation process is illustrated numerically for a deep tunnel in the CJPL-II project. By continuously monitoring the current strain energy at the bottom corner of the tunnel, we plot this value with respect to the distance between the monitoring section and working face (Fig. 52). In this figure, it shows that when the working face approaches the monitoring section, the energy first begins to increase with the excavation process and then decreases rapidly. Conceptually, if the accumulated energy of a rock mass reaches a specific threshold (usually determined by laboratory tests for rockburst proneness), violent energy release phenomena such as rockburst occur.

According to the understanding of the energy release capacity of hard rocks in deep engineering, the energy storage capacity and ductility of surrounding rock masses should be improved, while the brittleness should be reduced to avoid the sudden release of energy. The following measures can be adopted to prevent disasters by energy mitigation, as shown in Fig. 53 (Feng, 2017):

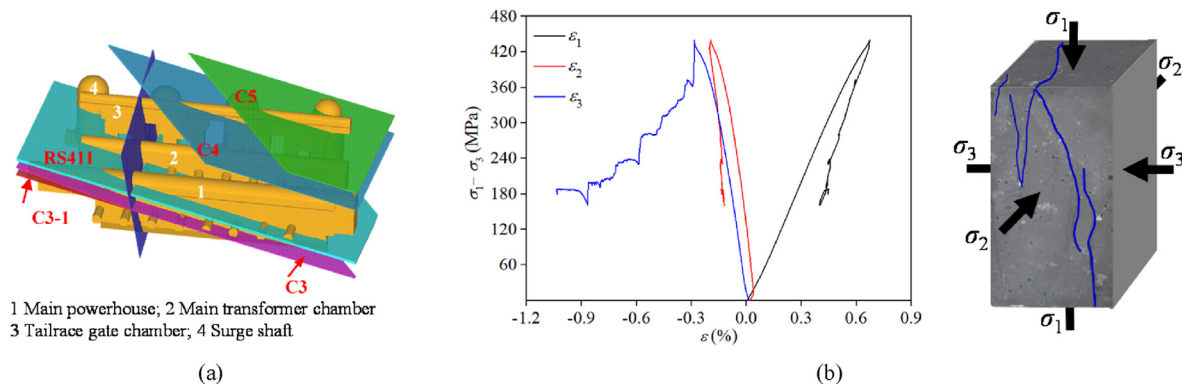


Fig. 54. Geological conditions of the right bank underground caverns of the Baihetan hydropower station: (a) Positional relationship between the ISZs and cavern group, and (b) Brittleness characteristics of the basalt.

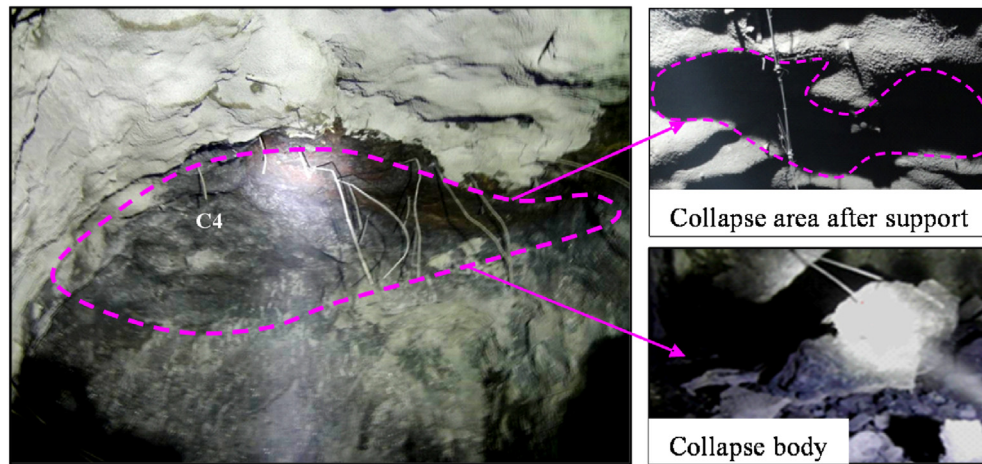


Fig. 56. Observed large-volume collapse due to ISZ of C4 of the underground powerhouse at the right bank (Duan et al., 2017).

Table 3

Reinforcement measures used for three typical failures.

Failure	Reinforcement measure
Spalling	(1) The layered excavation height is constrained to within 4 m; (2) The initial shotcrete thickness is increased to 8–12 cm; (3) The support time of rockbolts is advanced to be carried out 8–12 m from the tunnel face
Collapse	The excavation footage is reduced, the excavation sequence is optimized, and timely support of anchor cables, rockbolts, etc., are added
Deep fracturing	Anchor cables with sufficient length and prestressed rockbolts are added in the stress-concentration zone

- (1) Reduce the energy concentration by optimizing the shape and size of the cross-section, number and height of benches, excavation rate, position, shape and size of the pilot tunnel, etc.
- (2) Prerelease and transfer energy by optimizing the position, length and spacing of stress-release holes or by presplitting to reduce the level of storage energy in surrounding rocks.
- (3) Absorb energy via energy-absorbing supports, such as energy-absorbing rockbolts, which can transfer the strain energy of the rock mass into the strain energy of the support element, thus reducing the energy concentration and release rate of surrounding rocks.

8. Case studies

8.1. Underground powerhouse at the Baihetan hydropower station

The underground cavern groups of the Baihetan hydropower station are to date the largest underground hydroelectric caverns in the world, with the size of the main powerhouse being 438 m in length, 88.7 m in height, and 34 m in width. The maximum principal stress is 22–26 MPa with an orientation of N0°–20°E and a dip angle of 2°–11°. Five slightly inclined interlayer staggered zones (ISZs) of C3, C3-1, RS411, C4 and C5 outcrop in the upper part of the high wall, or arch, of the right bank caverns (Fig. 54a). The actual rock exposed in the underground cavern is mainly cryptocrystal basalt, which has characteristics of both hardness and brittleness, with a UCS of 120–150 MPa and a tensile strength of 10–15 MPa (Fig. 54b). The strength of basalt follows the 3D hard rock failure criterion (3DHRFC) (Fig. 55).

During the excavation of the underground powerhouse, three typical failures occurred: large-scale spalling (Fig. 14b and c), large-

scale collapse due to ISZs (Fig. 56) and deep fracturing of surrounding rocks (Fig. 18). Using the cracking-restraint method, reinforcement measures are proposed to control different rock mass failures (Table 3). Fig. 57 shows the evolution of rock fracturing depths with excavation process before and after the application of cracking-restraint method obtained through numerical simulation and field monitoring for the three typical failures. Ultimately, the spalling, collapse and deep fracturing are well controlled after taking corresponding reinforcement measures, and the rock fracturing depths gradually stabilize.

8.2. Deep railway tunnels excavated using the drill-and-blast method

A deep railway tunnel is considered that is ~13 km in length, with a maximum depth of over 2000 m and an in situ stress σ_1 of ~58 MPa (Hu et al., 2020). The tunnel was excavated by the full-face drill-and-blast method. The surrounding rocks are mainly integral and block structured. The surrounding rocks are medium-grained biotite monzogranite. The mechanical properties of the granite under different stress states are analyzed based on true triaxial tests. As shown in Fig. 58, the rock exhibits typical brittle failure characteristics. It has a higher strength under the true triaxial stress state, which increases with increasing σ_2 (Fig. 59). Its 3DHRFC criterion parameters are listed in Table 4.

It is estimated at the design stage that the length of rockburst zones is more than 10 km, and moderate or stronger rockburst zones are larger than 6 km in length. More than 400 rockbursts occurred during tunnel excavation. Fig. 60 shows a typical moderate rockburst case that occurred in this tunnel. The LERR evolution of rockbursts with different intensities during excavation is

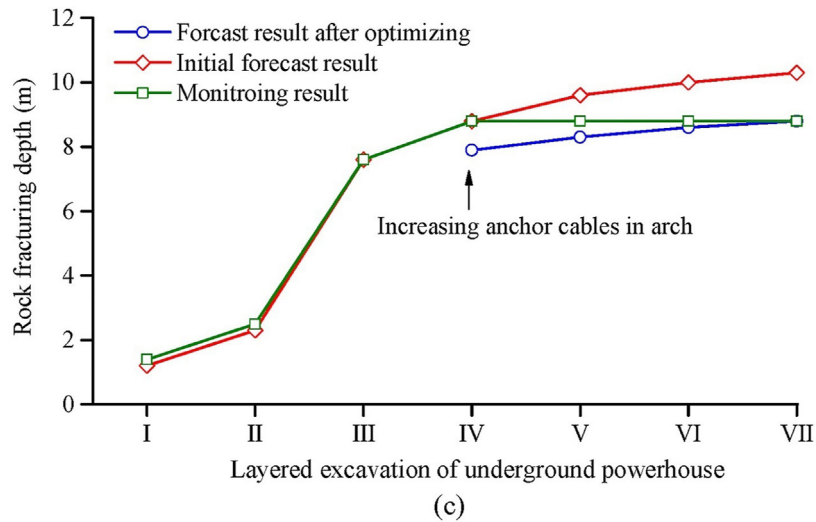
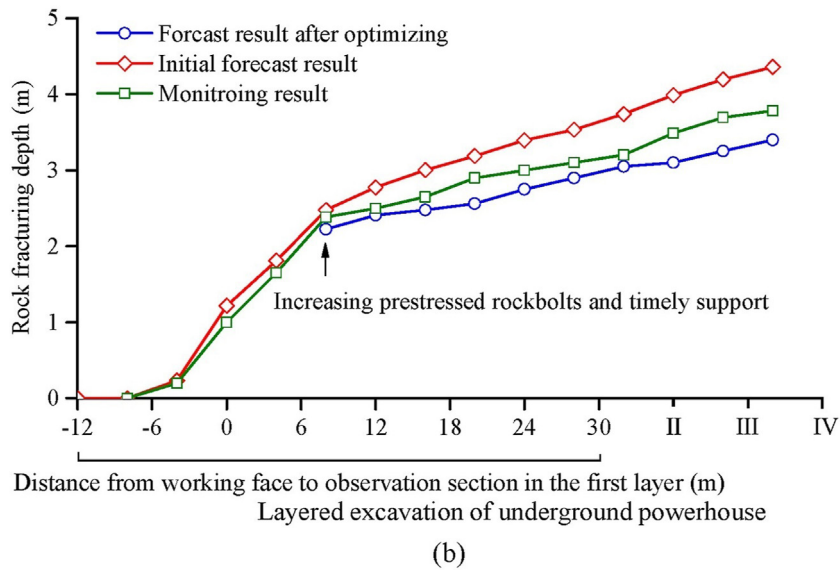
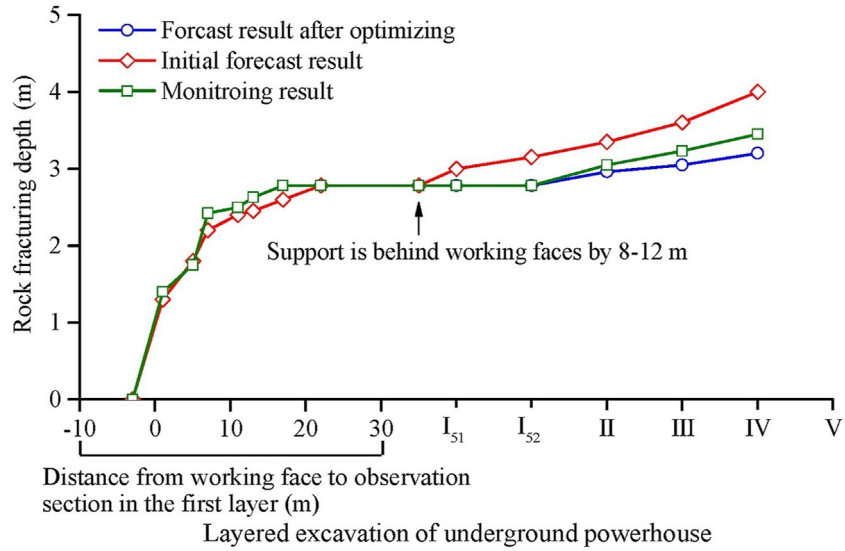


Fig. 57. Evolution of rock fracturing depths of the early forecast result, monitoring result and forecast result after optimizing measures are adopted for the three typical failures: (a) Rock spalling, (b) Collapse, and (c) Deep fracturing.

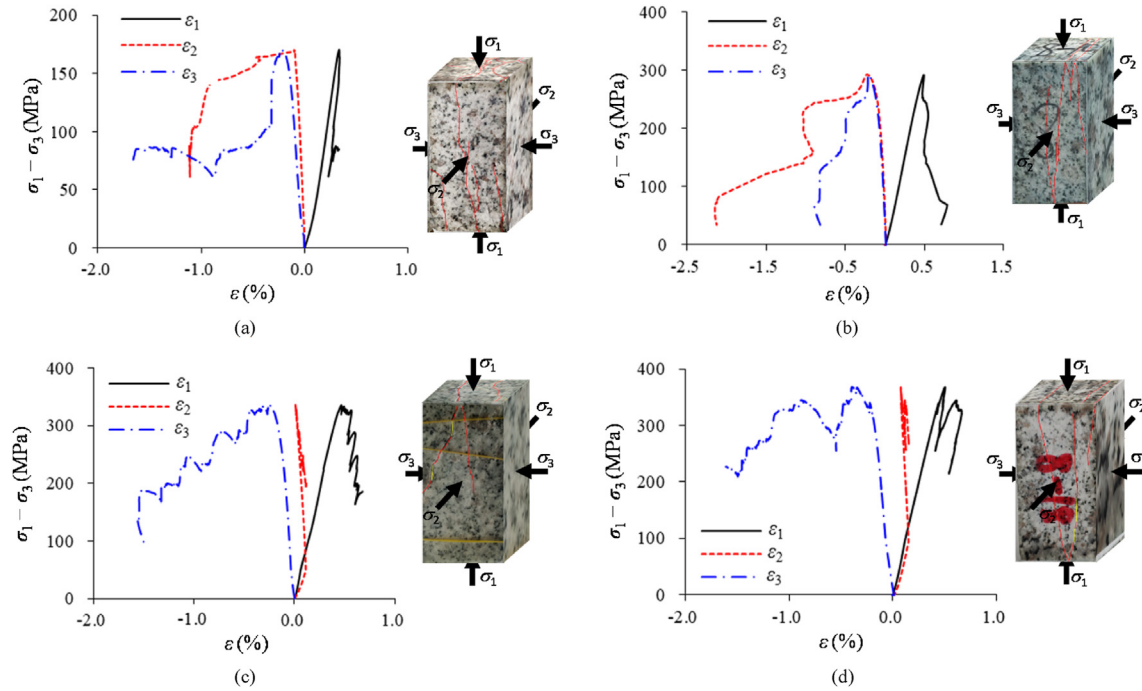


Fig. 58. Results of the true triaxial compression test on the granite around the tunnel: (a) $\sigma_3 = 0$ MPa, $\sigma_2 = 0$ MPa; (b) $\sigma_3 = 5$ MPa, $\sigma_2 = 5$ MPa; (c) $\sigma_3 = 5$ MPa, $\sigma_2 = 60$ MPa; and (d) $\sigma_3 = 5$ MPa, $\sigma_2 = 100$ MPa.

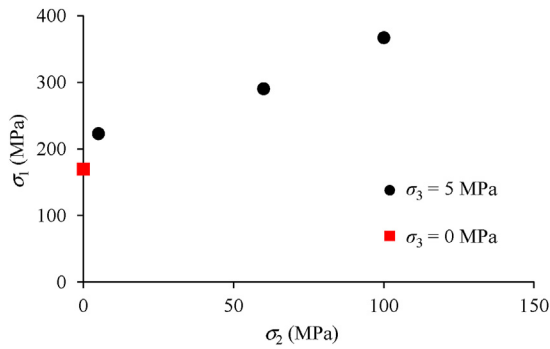


Fig. 59. True triaxial compressive strength of the granite under different stress states.

Table 4

Mechanical parameters of medium-grained biotite monzogranite in the 3D failure criterion.

c_0 (MPa)	φ_0 (°)	s	t
52	52	0.95	0.88

simulated and shown in Fig. 61. It can also be seen that the higher the rockburst intensity, the greater the energy accumulated during the development process.

According to the rockburst warning results, prevention and control methods of different intensities of rockbursts are established using the energy-controlled method. By analyzing the value of the microseismic release energy relative to the distance between the monitored section and the working face, the evolution characteristics of the surrounding rock energy with the excavation process are revealed, as shown in Fig. 62. On this basis, energy-controlled measures for rockburst mitigation were

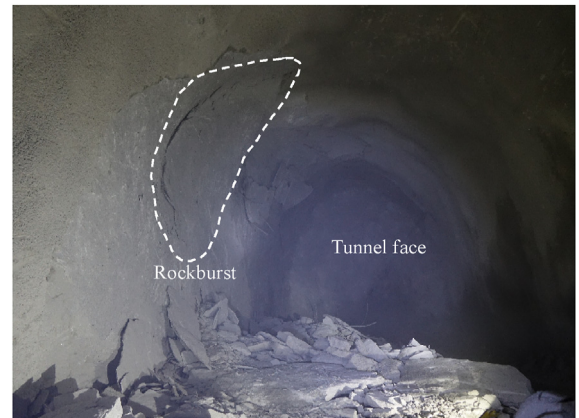


Fig. 60. Typical moderate rockburst case in the deep railway tunnel.

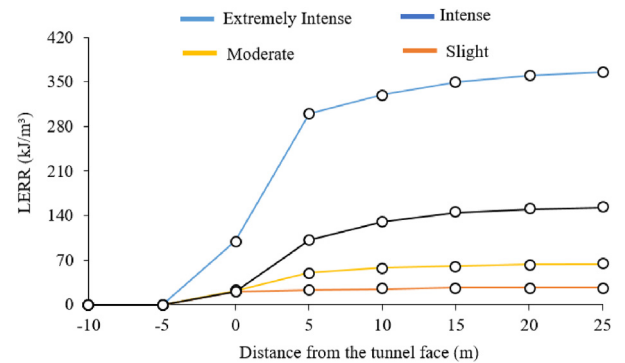


Fig. 61. Evolution of the LERR of surrounding rocks with excavation in areas of rockbursts with different intensities.

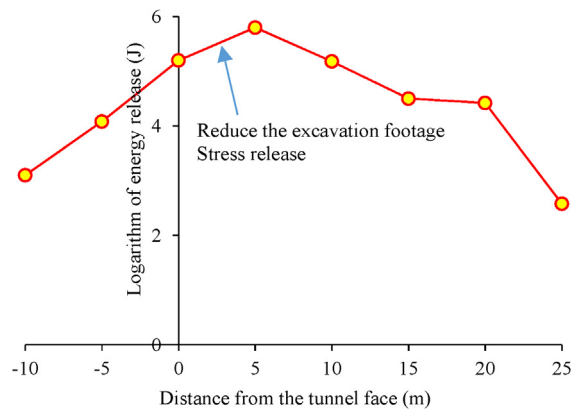


Fig. 62. Energy evolution curve with respect to the excavation process in the tunnel.

formulated and successfully applied in the tunnel, as shown in Table 5. Fig. 63a shows a typical control effect for a potential rockburst using an energy-absorbing bolt support. Ultimately, the rockburst disasters of the tunnel were greatly alleviated with lower support cost, and the construction efficiency was increased by 30% (Fig. 63b).

9. Concluding remarks and future directions

The disasters of deep hard rock engineering, including rock spalling, deep cracking, collapse, large deformation and rockburst, are mainly caused by the internal fracturing and energy release of surrounding rocks. A new rock mechanics research system with a focus on the excavation-induced deep hard rock fracturing process has been established, and significant progress has been made. Numerous testing techniques for determining the mechanical properties and

Table 5
Control measures for rockbursts with different intensities.

Rockburst warning intensity	Rockburst control measure
Intense	(1) Initiate immediate mitigation measures; (2) Perform the combination of postpone construction + stress-release hole + bolt, mesh and steel arch
Moderate	(1) Conduct timely mitigation measures; (2) Implement the stress-release hole, short footage, and bolt + mesh + steel arch. The combination of the two is implemented, and the latter two are optimized
Slight	(1) If the warning is slight for several times in a row, the mitigation measures should be taken in a timely manner. If the rockburst has occurred and the rockburst risk exhibits a downward trend, the mitigation measures can be postponed; (2) Implementation of a single mitigation measure is sufficient, i.e. stress-release hole or short footage or bolt + mesh
None	There is no need to take rockburst mitigation measures

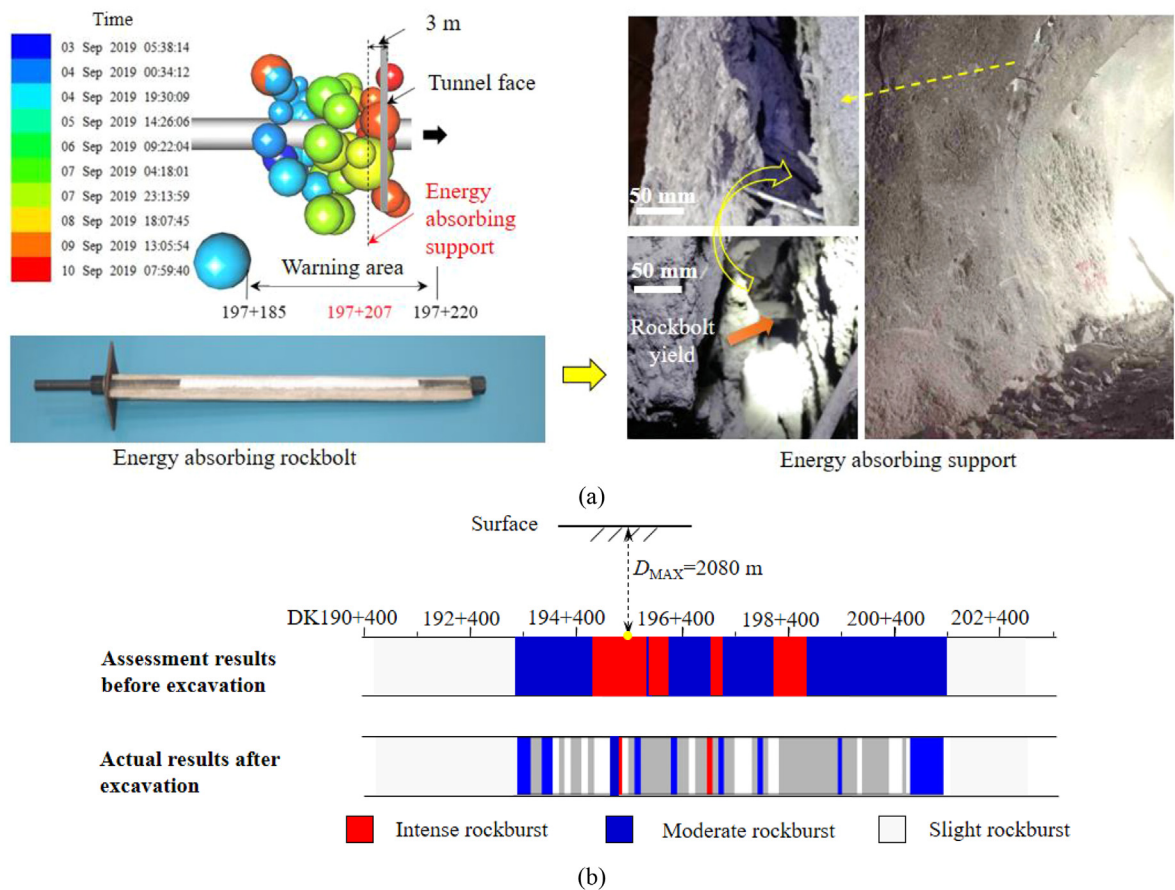


Fig. 63. Rockburst control: (a) Energy-absorbing support based on rockburst warning result, and (b) Comparison of rockburst sections before and after support.

fracturing process of hard rocks under true triaxial excavation stress paths have been developed. The evolution mechanisms of stress-induced deep hard rock fracturing and catastrophic processes have been deeply recognized, and the corresponding mechanical analysis theory, model and calculation method have been established. The new control design theory for deep hard rock fracturing and the energy accumulation and release process, cracking-restraint method and energy-controlled method have been proposed and successfully applied to engineering practice.

With the continuous development of deep rock engineering practices, the exposed engineering geological environment is becoming increasingly complex and new types of disasters are encountered. Following the research system proposed, further research focus can be directed as follows:

- (1) The development of a true triaxial rock mechanics testing apparatus and techniques considering high temperatures up to 400 °C–800 °C and high liquid pressures up to 70–100 MPa can provide a means for studying the effects of coupled high true triaxial stress, high temperature and high liquid pressure on the excavation-induced deep hard rock fracturing process.
- (2) More sophisticated rock failure mechanical models for deep hard rock excavation can be considered in terms of the effects of hard structural planes, time-dependent behavior, coupling processes of high temperature, high hydraulic liquid, high stresses, etc.
- (3) A 3D continuous-discontinuous analysis method can be considered that has large-scale fine simulation of the deep rock mass fracturing process and evolution process of stress-induced disasters.
- (4) Calculation and analysis methods and monitoring and early warning technology for large deformation of deep hard rocks are warranted.
- (5) Theories and techniques can be developed to improve production efficiency utilizing deep hard rock fracturing induced through high stress, high pressure, high temperature, etc.
- (6) More practical applications in deep rock engineering merit further consideration.

Declaration of competing interest

The authors declare that they have no known competing financial interests or personal relationships that could have appeared to influence the work reported in this paper.

Acknowledgments

The authors gratefully acknowledge financial support from the National Natural Science Foundation of China (Grant Nos. 51839003 and 41827806) and Liaoning Revitalization Talents Program of China (Grant No. XLYCYSZX1902). We thank Dr. Zhaofeng Wang, Dr. Shufeng Pei, Mr. Gang Wang, Mr. Qiang Han and Mr. Liangjie Gu for their help in writing this paper. The comments of Professors Qihu Qian, Yangsheng Zhao, Chunlin Li, Ming Cai, Qiang Yang, Xiaoping Zhou, Shigang She, Peng Lin and Quan Jiang greatly improved this paper.

References

Aydan, O., Akagi, T., Kawamoto, T., 1993. The squeezing potential of rocks around tunnels: theory and prediction. *Rock Mech. Rock Eng.* 26 (2), 137–163.
 Barton, N., Shen, B.T., 2017. Risk of shear failure and extensional failure around over-stressed excavations in brittle rock. *J. Rock Mech. Geotech. Eng.* 9 (2), 210–225.
 Chen, J.T., Feng, X.T., 2006. True triaxial experimental study on rock with high geostress. *Chin. J. Geotech. Eng.* 28 (8), 1537–1543 (in Chinese).

Duan, S.Q., Feng, X.T., Jiang, Q., Liu, G.F., Pei, S.F., Fan, Y.L., 2017. In situ observation of failure mechanisms controlled by rock masses with weak interlayer zones in large underground cavern excavations under high geostress. *Rock Mech. Rock Eng.* 50 (9), 2465–2493.
 Durrheim, R.J., Haile, A., Roberts, M.K.C., Schweitzer, J.K., Spottiswoode, S.M., Klokow, J.W., 1998. Violent failure of a remnant in a deep South African gold mine. *Tectonophysics* 289, 105–116.
 Fan, Q.X., Feng, X.T., Weng, W.L., Fan, Y.L., Jiang, Q., 2017. Unloading performances and stabilizing practices for columnar jointed basalt: a case study of Baihetan hydropower station. *J. Rock Mech. Geotech. Eng.* 9, 1041–1053.
 Faradonbeh, R.S., Taheri, A., Karakus, M., 2022. The propensity of the over-stressed rock masses to different failure mechanisms based on a hybrid probabilistic approach. *Tunn. Undergr. Space Technol.* 119, 104214.
 Feng, X.T., Pan, P.Z., Zhou, H., 2006. Simulation of the rock microfracturing process under uniaxial compression using an elasto-plastic cellular automaton. *Int. J. Rock Mech. Min. Sci.* 43 (7), 1091–1108.
 Feng, X.T., Hudson, J.A., 2011. *Rock Engineering Design*. CRC Press.
 Feng, X.T., Hao, X.J., Jiang, Q., Li, S.J., Hudson, J.A., 2016a. Rock cracking indices for improved tunnel support design: a case study for columnar jointed rock masses. *Rock Mech. Rock Eng.* 49 (6), 2115–2130.
 Feng, X.T., Zhang, X.W., Kong, R., Wang, G., 2016b. A novel Mogi type true triaxial testing apparatus and its use to obtain complete stress–strain curves of hard rocks. *Rock Mech. Rock Eng.* 49 (5), 1649–1662.
 Feng, X.T., 2017. *Rockburst: Mechanisms, Monitoring, Warning, and Mitigation*. Butterworth-Heinemann.
 Feng, X.T., Pei, S.F., Jiang, Q., Zhou, Y.Y., Li, S.J., Yao, Z.B., 2017. Deep fracturing of the hard rock surrounding a large underground cavern subjected to high geostress: in situ observation and mechanism analysis. *Rock Mech. Rock Eng.* 50 (8), 2155–2175.
 Feng, X.T., Xu, H., Qiu, S.L., Li, S.J., Yang, C.X., Guo, H.S., Cheng, Y., Gao, Y.H., 2018a. In situ observation of rock spalling in the deep tunnels of the China Jinping underground laboratory (2400 m depth). *Rock Mech. Rock Eng.* 51 (4), 1193–1213.
 Feng, X.T., Zhao, J., Zhang, X.W., Kong, R., 2018b. A novel true triaxial apparatus for studying the time-dependent behaviour of hard rocks under high stress. *Rock Mech. Rock Eng.* 51 (9), 2653–2667.
 Feng, X.T., Haimson, B., Li, X.C., Chang, C.D., Ma, X.D., Zhang, X.W., Ingraham, M., Suzuki, K., 2019a. ISRM suggested method: determining deformation and failure characteristics of rocks subjected to true triaxial compression. *Rock Mech. Rock Eng.* 52 (6), 2011–2020.
 Feng, X.T., Young, R.P., Reyes Montes, J.M., Aydan, O., Ishida, T., Liu, J.P., Liu, H.J., 2019b. ISRM suggested method for in situ acoustic emission monitoring of the fracturing process in rock masses. *Rock Mech. Rock Eng.* 52 (5), 1395–1414.
 Feng, X.T., Xiao, Y.X., Feng, G.L., Yao, Z.B., Chen, B.R., Yang, C.X., Su, G.S., 2019c. Study on the development process of rockbursts. *Chin. J. Rock Mech. Eng.* 38 (4), 649–673 (in Chinese).
 Feng, X.T., Kong, R., Zhang, X., Yang, C.X., 2019d. Experimental study of failure differences in hard rock under true triaxial compression. *Rock Mech. Rock Eng.* 52, 2109–2122.
 Feng, X.T., Kong, R., Yang, C.X., Zhang, X.W., Wang, Z.F., Han, Q., Wang, G., 2019e. A three-dimensional failure criterion for hard rocks under true triaxial compression. *Rock Mech. Rock Eng.* 53 (1), 103–111.
 Feng, X.T., Kong, R., Zhang, X., et al., 2021a. Technical Specification for True Triaxial Test of Rock Specimen. Chinese Society for Rock Mechanics and Engineering, Beijing, China (in Chinese).
 Feng, X.T., Wang, G., Zhang, X.W., Yang, C.X., Kong, R., Zhao, J., Xu, H., 2021b. Experimental method for direct shear tests of hard rock under both normal stress and lateral stress. *Int. J. Geomech.* 21 (3), 04021013.
 Feng, X.T., Zhao, J., Wang, Z.F., Yang, C.X., Han, Q., Zheng, Z., 2021c. Effect of high differential stress and mineral properties on deformation and failure mechanism of hard rocks. *Can. Geotech. J.* 58, 411–426.
 Feng, X.T., Wang, Z.F., Zhou, Y.Y., Yang, C.X., Pan, P.Z., Kong, R., 2021d. Modelling three-dimensional stress-dependent failure of hard rocks. *Acta. Geotech.* 16 (6), 1647–1677.
 Feng, X.T., Pan, P.Z., Wang, Z.F., Zhang, Y.L., 2021e. Development of cellular automata software for engineering rockmass fracturing processes. In: *Challenges and Innovations in Geomechanics*. Springer, pp. 62–74.
 Gao, Y.H., Feng, X.T., Wang, Z.F., Zhang, X.W., 2019. Strength and failure characteristics of jointed marble under true triaxial compression. *Bull. Eng. Geol. Environ.* 79 (2), 891–905.
 Hagan, T.O., Milev, A.M., Spottiswoode, S.M., Hildyard, M.W., Grodner, M., Rorke, A.J., Finnie, G.J., Reddy, N., Haile, A.T., Le Bron, K.B., Grave, D.M., 2001. Simulated rockburst experiment - an overview. *J. S. Afr. Inst. Min. Metall.* 101 (5), 217–222.
 Haimson, B., 2006. True triaxial stresses and the brittle fracture of rock. *Pure Appl. Geophys.* 163, 1101–1130.
 Hajiabdomajid, V., Kaiser, P.K., 2003. Brittleness of rock and stability assessment in hard rock tunnelling. *Tunn. Undergr. Space Technol.* 18, 35–48.
 Hajiabdomajid, V., Kaiser, P.K., Martin, C.D., 2002. Modeling brittle failure of rock. *Int. J. Rock Mech. Min. Sci.* 39, 31–741.
 Hamdi, J., Scholtès, L., Souley, M., Marwan, A.H., 2017. Effect of discretization at laboratory and large scales during discrete element modelling of brittle failure. *Int. J. Rock Mech. Min. Sci.* 100, 48–61.
 Han, Q., Feng, X.T., Yang, C.X., Kong, R., Zhao, J., Zhang, Y., 2021. Evaluation of the crack propagation capacity of hard rock based on stress-induced deformation anisotropy and the propagation angle of volumetric strain. *Rock Mech. Rock Eng.* 54, 6585–6603.

- Hatzor, Y.H., He, B.G., Feng, X.T., 2017. Scaling rockburst hazard using the DDA and GSI methods. *Tunn. Undergr. Space Technol.* 70, 343–362.
- He, M.C., Miao, J.L., Feng, J.L., 2010. Rock burst process of limestone and its acoustic emission characteristics under true-triaxial unloading conditions. *Int. J. Rock Mech. Min. Sci.* 47, 286–298.
- He, M.C., Qian, Q.H., 2010. *Foundation of Deep Rock Mass Mechanics*. Science Press, Beijing, China.
- Hoek, E., Guevara, R., 2009. Overcoming squeezing in the Yacambú-Quibor tunnel, Venezuela. *Rock Mech. Rock Eng.* 42 (2), 389–418.
- Hu, L., Feng, X.T., Xiao, Y.X., Wang, R., Feng, G.L., Yao, Z.B., Niu, W.J., Zhang, W., 2020. Effects of structural planes on rockburst position with respect to tunnel cross-sections: a case study involving a railway tunnel in China. *Bull. Eng. Geol. Environ.* 79 (2), 1061–1081.
- Ingraham, M.D., 2012. Investigation of Localization and Failure Behaviour of Castlegate Sandstone Using True Triaxial Testing. PhD Thesis. Clarkson University, New York, USA.
- Jiang, Q., Feng, X.T., Li, S.J., Su, G.S., Xiao, Y.X., 2019. Cracking-restraint design method for large underground caverns with hard rock under high geostress condition and its practical application. *Chin. J. Rock Mech. Eng.* 38 (6), 1081–1101 (in Chinese).
- Kaiser, P.K., Moss, A., 2021. Deformation-based support design for highly stressed ground with a focus on rockburst damage mitigation. *J. Rock Mech. Geotech. Eng.* <https://doi.org/10.1016/j.jrmge.2021.05.007>.
- Kong, R., Feng, X.T., Zhang, X.W., Yang, C.X., 2018. Study on crack initiation and damage stress in sandstone under true triaxial compression. *Int. J. Rock Mech. Min. Sci.* 106, 117–123.
- Kusui, A., Villaescusa, E., Funatsu, T., 2016. Mechanical behavior of scaled-down unsupported tunnel walls in hard rock under high stress. *Tunn. Undergr. Space Technol.* 60, 30–40.
- Kwasniewski, M., 2007. Mechanical behavior of rocks under true triaxial compression conditions - volumetric strain and dilatancy. *Arch. Min. Sci.* 52, 409–435.
- Langford, J.C., Diederichs, M.S., 2015. Reliable support design for excavations in brittle rock using a global response surface method. *Rock Mech. Rock Eng.* 48 (2), 669–689.
- Li, C.C., 2017. Principles of rockbolting design. *J. Rock Mech. Geotech. Eng.* 9 (3), 396–414.
- Li, X.B., Du, K., Li, D.Y., 2015. True triaxial strength and failure modes of cubic rock specimens with unloading the minor principal stress. *Rock Mech. Rock Eng.* 48, 2185–2196.
- Li, Z.K., Zhou, Z., Tang, X.F., Liao, C.G., Hou, D.Q., Xing, X.L., Zhang, Z.Z., Liu, Z.G., Chen, Q.H., 2009. Stability analysis and considerations of underground powerhouse caverns group of Jinping I hydropower station. *Chin. J. Geotech. Eng.* 28 (11), 2167–2175 (in Chinese).
- Lin, Y.M., 1983. Displacement evolution of deep tunnel near the ore body. *Chin. J. Geotech. Eng.* 2 (1), 89–102 (in Chinese).
- Liu, G.F., Feng, X.T., Jiang, Q., Yao, Z.B., Li, S.J., 2017. In situ observation of spalling process of intact rock mass at large cavern excavation. *Eng. Geol.* 226, 52–69.
- Louchnikov, V.N., Eremenko, V.A., Sandy, M.P., Kosyrev, M.A., 2017. Support design for mines exposed to rockburst hazard. *J. Min. Sci.* 53 (3), 504–512.
- Lu, B., Wang, J.M., Ding, X.L., Wu, A.Q., Duan, S.H., Huang, S.L., 2010. Study of deformation and cracking mechanism of surrounding rock of Jinping I underground powerhouse. *Chin. J. Rock Mech. Eng.* 29 (12), 2429–2441 (in Chinese).
- Luke, P.F., Jesse, H., Marte, G., Tutuncu, A., Mattson, E., 2019. Patterns in complex hydraulic fractures observed by true triaxial experiments and implications for proppant placement and stimulated reservoir volumes. *J. Pet. Explor. Prod. Technol.* 9, 2781–2792.
- Martin, C.D., Christiansson, R., 2009. Estimating the potential for spalling around a deep nuclear waste repository in crystalline rock. *Int. J. Rock Mech. Min. Sci.* 46 (2), 219–228.
- Malan, D.F., Napier, J.A.L., 2018. Rockburst support in shallow-dipping tabular stopes at great depth. *Int. J. Rock Mech. Min.* 112, 302–312.
- Mercier-Langevin, F., Hadjigeorgiou, J., 2013. Towards a better understanding of squeezing potential in hard rock mines. *Min. Technol.* 120 (1), 36–44.
- Milev, A.M., Spottiswoode, S.M., Rorke, A.J., Finnie, G.J., 2001. Seismic monitoring of a simulated rockburst on a wall of an underground tunnel. *J. S. Afr. Inst. Min. Metall.* 101 (5), 253–260.
- Miranda, T., Dias, D., Eclaircy-Caudron, S., Correia, A.G., Costa, L., 2011. Back analysis of geomechanical parameters by optimization of a 3D model of an underground structure. *Tunn. Undergr. Space Technol.* 26 (6), 659–673.
- Ortlepp, W.D., Stacey, T.R., 1994. Rockburst mechanisms in tunnels and shafts. *Tunn. Undergr. Space Technol.* 9, 59–65.
- Ortlepp, W.D., 2005. RaSiM comes of age – a review of the contribution to the understanding and control of mine rockburst. In: *Proceeding of the 6th International Symposium on Rockburst and Seismicity in Mines*. Australian Centre for Geomechanics, pp. 3–20.
- Qian, Q.H., Lin, P., 2016. Safety risk management of underground engineering in China: progress, challenges and strategies. *J. Rock Mech. Geotech. Eng.* 8 (4), 423–442.
- Qian, Q.H., Zhou, X.P., 2011. Quantitative analysis of rockburst for surrounding rocks and zonal disintegration mechanism in deep tunnels. *J. Rock Mech. Geotech. Eng.* 3 (1), 1–9.
- Qian, Q.H., Zhou, X.P., 2018. Failure behaviors and rock deformation during excavation of underground cavern group for Jinping I hydropower station. *Rock Mech. Rock Eng.* 51, 2639–2651.
- Rajmeny, P.K., Singh, U.K., Sinha, B.K.P., 2002. Predicting rock failure around boreholes and drives adjacent to stops in Indian mines in high stress regions. *Int. J. Rock Mech. Min. Sci.* 39, 151–164.
- Read, R.S., 2004. 20 years of excavation response studies at AECL's Underground Research Laboratory. *Int. J. Rock Mech. Min. Sci.* 41, 1251–1275.
- Song, S.W., Feng, X.M., Liao, C.G., Liu, Z., Yang, Y., 2016. Measures for controlling large deformations of underground caverns under high in-situ stress condition: a case study of Jinping I hydropower station. *J. Rock Mech. Geotech. Eng.* 8 (5), 605–618.
- Su, G.S., Feng, X.T., Jiang, Q., Chen, G.Q., 2006. Study on new index of local energy release rate for stability analysis and optimal design of underground rockmass engineering with high geostress. *Chin. J. Rock Mech. Eng.* 25 (12), 2453–2460 (in Chinese).
- Su, G.S., Shi, Y.J., Feng, X.T., Jiang, J., Zhang, J., Jiang, Q., 2018. True triaxial experimental study of the evolutionary features of the acoustic emissions and sounds of rockburst processes. *Rock Mech. Rock Eng.* 51, 375–389.
- Tiwari, R.P., Rao, K.S., 2006. Deformability characteristics of a rock mass under true-triaxial stress compression. *Geotech. Geol. Eng.* 24, 1039–1063.
- Trinh, N., Jonsson, K., 2013. Design considerations for an underground room in a hard rock subjected to a high horizontal stress field at Rana Gruber, Norway. *Tunn. Undergr. Space Technol.* 38, 205–212.
- Vazaios, I., Vlachopoulos, N., Diederichs, M.S., 2019. Assessing fracturing mechanisms and evolution of excavation damaged zone of tunnels in interlocked rock masses at high stresses using a finite-discrete element approach. *J. Rock Mech. Geotech. Eng.* 11 (4), 701–722.
- Wang, P., Jin, K., Song, G., Zhang, Y.L., 2017. Discussion on relaxation zone characteristics of columnar jointed basaltic rock in large underground cavern and the treatment measures. *Geotech. Invest. Survey* 45 (2), 31–36 (in Chinese).
- Williams, T.J., Wideman, C.J., Scott, D.F., 1992. Case history of a slip-type rockburst. *Pure Appl. Geophys.* 139 (3/4), 627–637.
- Xia, Y.L., Peng, S.Z., Gu, Z.Q., Ma, J., 2007. Stability analysis of an underground power cavern. *Tunn. Undergr. Space Technol.* 22, 161–165.
- Xiao, Y.X., Feng, X.T., Hudson, J.A., Chen, B.R., Feng, G.L., Liu, J.P., 2016. ISRM suggested method for in situ microseismic monitoring of the fracturing process in rock masses. *Rock Mech. Rock Eng.* 49 (1), 343–369.
- Xie, H.P., Gao, F., Ju, Y., 2015. Research and development of rock mechanics in deep ground engineering. *Chin. J. Rock Mech. Eng.* 34 (11), 2161–2178 (in Chinese).
- Xie, H.P., 2021. *Deep Rock Mechanics and Mining Theory*. Science Press, Beijing, China.
- Xu, H., Feng, X.T., Yang, C., Zhang, X., Zhou, Y., Wang, Z., 2019. Influence of initial stresses and unloading rates on the deformation and failure mechanism of Jinping marble under true triaxial compression. *Int. J. Rock Mech. Min. Sci.* 117, 90–104.
- Zhang, X.B., 2010. Research and practice of the roof collapse treatment in Dagangshan hydropower station powerhouse. *Sichuan Water Power* 29 (6), 55–59 (in Chinese).
- Zhao, J., Feng, X.T., Zhang, X.W., Zhang, Y., Zhou, Y.Y., Yang, C.X., 2018. Brittle-ductile transition and failure mechanism of Jinping marble under true triaxial compression. *Eng. Geol.* 232, 160–170.
- Zhao, J., Feng, X.T., Yang, C.X., Zhou, Y.Y., Zhang, Y., 2021a. Study on time-dependent fracturing behaviour for three different hard rocks under high true triaxial stress. *Rock Mech. Rock Eng.* 54 (3), 1239–1255.
- Zhao, J., Feng, X.T., Yang, C.X., Zhang, X.W., Jiang, M.F., 2021b. Differential time-dependent fracturing and deformation characteristics of Jinping marble under true triaxial stress. *Int. J. Rock Mech. Min. Sci.* 138, 1–17.
- Zhao, J., Feng, X.T., Yang, C.X., He, B.G., Jiang, M.F., 2021c. Relaxation behaviour of Jinping marble under high true-triaxial stresses. *Int. J. Rock Mech. Min. Sci.* <https://doi.org/10.1016/j.jrmms.2021.104968>.
- Zhao, J.S., Feng, X.T., Jiang, Q., Zhou, Y.Y., 2018. Microseismicity monitoring and failure mechanism analysis of rock masses with weak interlayer zone in underground intersecting chambers: a case study from the Baihetan Hydropower Station, China. *Eng. Geol.* 245, 44–60.



Prof. Xia-Ting Feng received his PhD degree at Northeastern University of Technology (namely Northeastern University since 1993), China in 1992 and then took the position of lecturer, associate professor and professor at the same university. He joined Institute of Rock and Soil Mechanics, Chinese Academy of Sciences (CAS) in 1998 as a Professor of Hundred Talent Program of the CAS and as Deputy Director in Charge and Director in 2001–2005. He has worked as Director of State Key Laboratory of Geomechanics and Geotechnical Engineering since 2007. He works at Northeastern University, China as a Vice President since September 2017. In February 2021, he became president of Northeastern University. He is President of Federation of International Geo-engineering Societies – FedIGS, President of International Society for Rock Mechanics (ISRM) Commission on Design Methodology, member of ISRM Commission on Testing Methods, and President of Chinese Society for Rock Mechanics and Engineering (CSRME). He was the past President of ISRM 2011–2015. He is also Editor-in-Chief of *Journal of Rock Mechanics and Geotechnical Engineering (JRMGE)* and *Chinese Journal of Rock Mechanics and Engineering*, and Associate Editor-in-Chief of *Chinese Journal of Theoretical and Applied Mechanics*. He is member of Editorial Board of *Rock Mechanics and Rock Engineering*. His research interests cover rock mechanics for deep rock engineering. He published more than 180 technical papers and the English book “*Rock Engineering Design*” and “*Rock Engineering Risk*” with Professor John Hudson. He has edited five volumes of the book “*Rock Mechanics and Rock Engineering*” (CRC Press) and the book “*Rockburst*” (Elsevier).